**Title**

Quantitative proteomics and transcriptomics exploration of primary myeloid cells: importance of ß tubulin isotypes for bone resorption.

**Running title**

Primary myeloid cell omics and tubulin isotypes

David Guérit[1,2*], Pauline Marie[1,2*], Anne Morel[1,2], Justine Maurin[1,2], Christel Verollet[3,4], Brigitte Raynaud-Messina[3,4], Serge Urbach[5], Anne Blangy[1,2@]

[1] Centre de Recherche de Biologie Cellulaire de Montpellier (CRBM), CNRS UMR 5237, 1919 route de Mende, 34293 Montpellier cedex 5, France.

[2] Montpellier University, 34095 Montpellier cedex 5, France.

[3] Institut de Pharmacologie et Biologie Structurale, IPBS, Université de Toulouse, CNRS, UPS, Toulouse, France

[4] International associated laboratory (LIA) CNRS "IM-TB/HIV" (1167), Toulouse, France and Buenos Aires, Argentina

[5] Functional Proteomics Facility, Institute of Functional Genomics, 141 rue de la Cardonille, 34000 Montpellier, France.

* Equal contribution, alphabetic order

@ Corresponding author:

Anne Blangy

Centre de Recherche de Biologie Cellulaire de Montpellier (CRBM),

CNRS UMR 5237,

1919 route de Mende, 34293 Montpellier cedex 5,

France.

Email : anne.blangy@crbm.cnrs.fr

Tel : +33 43435 9508

**Key words**

Osteoclast, Tubulin, SILAC, RNAseq, Myeloid cell, Tubb6

**Summary statement**

This study provides original proteomic and transcriptomic data of primary myeloid cells. The analysis led to signatures for osteoclasts and for immature dendritic cells including potential new regulators of their specific biology. RNA interference showed in particular that ß tubulin isotype Tubb6 participates in osteoclast podosome patterning and in resorption activity.

**Abstract**

In the hematopoietic lineage, osteoclasts (Oc) and immature dendritic cells (Dc) are closely related myeloid cell types that fulfill very distinct biological functions; Oc participate in maintaining skeleton health while Dc sample the environment for foreign antigens. These morphological and functional specificities are based on the profound modification of gene and protein expression that occur during Oc and Dc differentiation. Here we provide global proteomic and transcriptomic analysis of primary mouse Oc, Dc and bone marrow macrophages based on original SILAC and RNAseq data obtained in a homogeneous experimental system. In particular, we established specific signatures for Oc and Dc that contain species of unknown functions, on top of the expected differentiation markers of each cell type. By siRNA screening, we highlighted potential new regulators of Oc biology. We also show that Oc, Dc and Mo have the same repertoire of 4 α and 4 β tubulin isotypes, but that Oc express much higher levels of Tubb6. We demonstrate that elevated expression of Tubb6 in Oc is necessary for the correct organization of podosomes into a belt, which is the backbone of the bone resorption apparatus, and that this function is conserved in human Oc. Consistently, we found that lowering Tubb6 expression hinders Oc resorption activity. Overall, our study highlights potential new regulators of Oc and Dc biology and it illustrates the functional importance of the tubulin isotype repertoire in the biology of differentiated cells.

## Introduction

Osteoclasts (Oc) and monocyte-derived immature dendritic cells (Dc) are closely related cell types belonging to the monocyte lineage of myeloid hematopoietic cells. Although closely related and capable of trans-differentiation (Madel et al., 2019), Oc and Dc fulfill very distinct biological functions. On one hand, Oc reside in the bone tissue and are specialized for bone resorption; they ensure the maintenance of bone health in coordination with osteoblasts, the bone forming cells. Oc function is also crucial for hematopoietic stem cell mobilization and they are closely linked with the immune system (Cappariello et al., 2014). On the other hand, immature dendritic cells are sentinels of the immune system that reside in peripheral tissues where they constantly sample the surrounding environment for pathogens, such as viruses or bacteria; upon non-self body encountering, Dc mature or differentiate into antigen presenting cells to fulfill their immune-initiating function (Tiberio et al., 2018). Myeloid cell differentiation is associated with the expression of distinctive proteins related to their specific functions, such as the Cathepsin K and the metalloprotease MMP9 in Oc for bone collagen fiber degradation (Cappariello et al., 2014) or the chemokine CCL17 in Dc for their migration and T cell chemo-attraction (Real et al., 2004). In particular, Oc have a very specific capacity to organize their actin cytoskeleton into a belt of podosomes, which is the backbone of the bone resorption apparatus (Georgess et al., 2014a; Touaitahuata et al., 2014), whereas Dc display clusters of podosomes that participate in antigen sampling (Baranov et al., 2014).

Unraveling the fine molecular mechanisms controlling the specific functions of Oc and Dc is key to understand the homeostasis and pathological dysfunctions of the bone and immune system homeostasis, and then to design targeted genetic and

pharmacological therapeutic strategies. In fact, improving knowledge about Dc biology and pathology paved the way for the manipulation of DCs to enhance immune responses, in particular in the context of cancer immunotherapy (Sabado et al., 2017; Wculek et al., 2019). The exacerbated activity of Oc causes osteoporosis, a serious public health problem leading to significant morbidity and mortality; this abnormal increase in Oc activity is associated with a number of pathologies ranging from age-related sexual hormone decay to chronic inflammation and cancer (Khosla and Hofbauer, 2017). Better understanding of Oc biology allowed to envision more focused therapeutic solutions against osteoporosis, as demonstrated by the recent approval of Denosumab, an antibody against the Receptor Activator of NF-κB Ligand (RANKL), the key cytokine for Oc differentiation (Compston et al., 2019) and the promising targets Cathepsin K (Drake et al., 2017) or Dock5 (Vives et al., 2015).

Differential proteomics and transcriptomics proved powerful tools to identify molecular pathways involved in specific cell functions. The comparison between Oc and Dc transcripts indeed revealed new regulators of bone resorption by Oc (Gallois et al., 2010; Georgess et al., 2014b) and combined Oc transcriptomics and proteomics shed light to the changes in cellular functions associated with Oc differentiation (An et al., 2014). Nevertheless, the very few studies available in myeloid cells are difficult to compare due to different cellular systems and experimental set up. Furthermore, the only proteomics data available for Oc were obtained with Oc derived from the RAW264.7 cell line, which proved to be very different from primary Oc, in particular regarding cytoskeleton regulation (Ng et al., 2018) that is key for bone resorption (Georgess et al., 2014a; Touaitahuata et al., 2014) and a promising therapeutic target against osteoporosis (Vives et al., 2015).

To overcome the limitation of currently available data, we provide here comparative quantitative proteomics and transcriptomics data of primary Oc, Dc and bone marrow macrophages (Mo), differentiated *ex vivo* from the same bone marrow cells. By minimalizing the culture condition differences to the cytokine cocktails used to differentiate each myeloid cell type, we could establish transcriptomic and proteomic signatures for Oc and Dc. We then exploited the data to uncovered potential new regulators of Oc biology and highlighted the ß-tubulin isotype Tubb6 determinant for Oc actin cytoskeleton organization and bone resorption capacity.

## Results

### *Global proteome and transcriptome of primary myeloid cells.*

Osteoclasts (Oc) and immature dendritic cells (Dc) are myeloid cells that perform very distinct biological functions. In order to get new insight into the molecular mechanisms underlying their specific activities, we sought to compare the global proteome and transcriptome of primary Oc and Dc, using bone marrow macrophages (Mo) as reference monocytic myeloid cell type. For this and to minimize irrelevant variations due to culture conditions, we set up conditions to derive the three myeloid cell types from the same mouse bone marrow cells with the only variation in culture medium composition being restricted to cytokines: GM-CSF for Dc, M-CSF for Mo and M-CSF + RANKL for Oc (Fig. 1A-B). In each experiment, we monitored Dc and Oc differentiation during and at the end of differentiation by controlling cell morphology and the cytoskeleton using phase-contrast and fluorescence microscopy (Fig. S1A-B).

To quantify proteins, we performed SILAC with isotope-labeled Arg and Lys: heavy-isotopic labeling (H) for Oc, intermediate-isotopic labeling (M) for Dc and no isotopic labeling (L) for Mo (Fig. 1A), incorporating isotope-labeled aminoacids at the time of cytokines addition in order to label only proteins neosynthetized during Dc and Oc differentiation. Protein levels were compared between Oc versus (vs) Mo (H+L), Dc vs Mo (M+L) and Oc vs Dc (H+M). To quantify transcripts, we performed RNAseq in identical culture conditions as SILAC except for labeled amino acids (Fig. 1B). Principal component analysis showed that SILAC and RNAseq biological replicates were grouped whereas the 3 SILAC clusters (H+L, M+L and H+M) and the

3 RNAseq clusters (Oc, Dc and Mo) were clearly separate (Fig. S2A-B), as confirmed by multi scatter plotting (Fig. S3-4). We further used these global SILAC and RNAseq data to identify the proteomic and transcriptomic specificities of primary Oc and Dc.

SILAC identified a total of 2,820 protein groups considering one peptide for adequate protein identification, among which 2,793 corresponded unambiguously to a single UniProt identifier and to a single protein; on the other hand 27 groups could not be resolved because they corresponded to several UniProt identifiers or a single UniProt identifier corresponded to several genes (Table S1). Among the 2,793 proteins, 1,959 were present in all three myeloid cell comparisons, 532 were in only 2 and 302 proteins were present in only one (Fig. 1A). The normalized $\log_2$ protein abundance ratios ranged between 6.9 (tartrate-resistant acid phosphatase type 5) and -6.4 (myoblast determination protein 1) in the Oc vs Mo comparison, between 7.4 (tartrate-resistant acid phosphatase type 5) and -6.5 (mucosa of esophagus-specific gene 1 protein) in for Oc vs Dc and between 6.1 (S100-A9) and -7.3 (piccolo) for Dc vs Mo (Fig. 1C and Table S1). Considering only genes annotated as "protein coding" in the Ensembl database, the RNAseq identified 15,597 mouse Ensembl genes in Oc; 16,197 in Dc and 15,875 in Mo, representing collectively 17,199 different genes. Most of the transcripts (14,663) were present in the three myeloid cell types as expected, whereas 1,144 were in only 2 and 1,392 transcripts were in only one (Fig. 1B and Table S2). Differential expression analysis of the 4 replicate experiments picked 4,781 transcript differences in Oc vs Mo, 6,903 in Oc vs Dc and 6,766 in Dc vs Mo (padj < 0.05 in Table S2). The $\log_2$ expression fold change ranged between 9.7 (calcitonin receptor) and -6.5 (solute carrier organic anion transporter family, member 2b1) for Oc vs Mo, between 9.7 (STEAP family member 4) and -10.4 (neutrophilic granule protein) for Oc vs Dc and between 10.3 (interleukin 33) and -8.5 (folate receptor 2) for

Dc vs Mo (Fig. 1D and Table S2). To establish the gene expression profiles, we excluded the 7,624 genes with the same expression levels in Oc, Dc and Mo (padj ≥ 0.05 in the three comparisons, italic in Table S2). We also excluded 540 genes whose mean expression levels were below 10 Fragments Per Kilobase Million (FPKM) in the three cell types (italic in Table S2). The 9,035 genes left were analyzed by hierarchical clustering, revealing 5 different clusters, corresponding to different gene expression profiles between Oc, Dc and Mo, in particular cluster E corresponding to elevated expression in Oc and clusters A and C to elevated expression in Dc (Fig. 2).

***Analysis of differential protein and gene expression between myeloid cells.***

We then identified proteins and genes characteristic of Oc and of Dc. For protein, we considered that the expression levels as different between cell types when the normalized $\log_2$ abundance ratio was ≥ 0.75 or ≤-0.75. Thereby, we established an Oc protein signature of 145 proteins for which protein levels were higher in Oc as compared both Dc and Mo (blue boxes in Fig. 3A, protein list in Table 1). Similarly, the immature Dc signature comprised 182 proteins (yellow boxes in Fig. 3A, protein list in Table S3). Conversely, 83 proteins were less abundant in Oc as compared both Dc and Mo (red boxes in Fig. 3A, protein list in Table S4) and 147 proteins were less abundant in Dc (grey boxes in Fig. 3A, protein list in Table S5). We performed a similar analysis for the 9,035 differentially expressed genes analyzed by hierarchical clustering, considering all transcripts with statistically significant changes (p adj<0.05 in Table S2). The Oc transcriptional signature contained 1,207 genes (blue highlight in Fig. 3B and Table S2) and the Dc one 2,419 genes (yellow highlight in Fig. 3B and

Table S2). Regarding the less expressed genes, we identified 554 genes less expressed in Oc (red highlight in Fig. 3B and Table S2) and 1,587 genes less expressed in Dc (grey highlight in Fig. 3B and Table S2).

When examining the correlation between proteomics and transcriptomics for the 2,793 proteins we identified by SILAC (Table S1), we found the rather low $R^2$ correlation coefficients (Fig. 3C). These values are in agreement with the correlations between RNA and protein expression observed previously in various biological and experimental systems (Ghazalpour et al., 2011), including Oc derived from the RAW264.7 cell line (An et al., 2014). In fact, among the 145 proteins of the Oc signature, only 72 genes were also in the Oc transcriptional signature whereas 2 genes were repressed (Table 1, pink and purple respectively) and 71 varied not significantly or differentially as compared to Dc or to Mo. Similarly, among the 182 proteins of the immature Dc signature, 139 genes were also in the transcriptional signature whereas 5 genes were repressed (Table S3, pink and purple respectively) and 38 varied not significantly or differentially as compared to Oc or to Mo. Thus, only half of the proteins in the Oc signature showed a correlated regulation of the transcript, the other half would not have been highlighted based on the sole RNAseq, including TREM2 and Tns3, two regulators of osteoclast differentiation and activity (Humphrey et al., 2006; Touaitahuata et al., 2016). Conversely, RNAseq provided a much deeper view of genes regulated during Oc and Dc differentiation, including genes essential for the bone resorption process such as Siglec15 (Hiruma et al., 2013), Bcar1 (Nagai et al., 2013) and Calcr (Turner et al., 2011), for which the proteins were not detected in SILAC.

Finally, we examined the molecular function (MF) and biological process (BP) GO terms associated with Oc and Dc signatures. As proteome and transcriptome

references, we used the 2,793 proteins identified by SILAC and the 17,199 genes identified by RNAseq respectively. In the Oc protein signature, all enriched GO terms were associated with energy metabolism by the mitochondria (Fig. 4A and Table S6), in agreement with the up-regulation of the metabolic enzymes of the tricarboxylic acid cycle during osteoclastogenesis and elevated energy metabolism in Oc (An et al., 2014; Lemma et al., 2016). At the transcriptional level, some enriched GO terms in Oc also pointed at mRNA translation (Fig. 4B and Table S7). For Dc signatures, all enriched GO terms related to the immune system (Fig. 4C-D and Tables S8-9). Consistent with the Oc GO term analysis, the main protein-protein interaction (PPI) networks built from the Oc transcriptional signature were 2 networks linked to mRNA translation (Fig. 4E-F) and one to mitochondrial energy production and translation (Fig. 4G).

Overall, the proteomic and transcriptomic approaches in primary myeloid cells proved complementary to identify biologically relevant species characteristic Oc and Dc. Moreover, the Oc and Dc signatures highlighted species of unknown function in these cell types, which could bring novel insights into the specific biological functions of these myeloid cells.

### *Identification of potential new regulators of Oc biology*

The 145 proteins of the Oc signature comprised 27 known regulators of Oc differentiation and activity (green highlight in Table 1) including cathepsin K and tartrate-resistant acid phosphatase type 5 (Cappariello et al., 2014), the vATPase complex, a3 subunit Tcirg1 (Ochotny et al., 2011) and Dock5 (Vives et al., 2011; Vives et al., 2015) as well as the Oc differentiation inhibitory proteins TRAF family

member-associated NF-kappa-B activator (TANK) (Maruyama et al., 2012) and Kbtbd11 (Narahara et al., 2019). There were also vATPase subunits, mitochondrial proteins in particular involved in oxidative phosphorylation and proteins involved in mRNA translation. Interestingly, there were also 45 proteins of unknown function in Oc (light and dark blue highlight in Table 1), in particular some involved in cytoskeleton and intracellular trafficking, two cellular processes key for bone resorption (Cappariello et al., 2014). Conversely, the 83 proteins less abundant in Oc comprised 7 known inhibitors of Oc differentiation or function (green highlight in Table S4) such as Pedf/Serpinf1, involved in human type VI osteogenesis imperfecta (Homan et al., 2011) and Fkbp5 associated with human Paget's disease (Lu et al., 2017). So far, the other 76 proteins have not been linked to Oc biology and could represent new Oc inhibitors (Table S4).

We then compared our data to the only SILAC Oc global proteomic analysis available so far, which studied osteoclastogenesis in RAW 264.7 cells (An et al., 2014). RAW 264.7 cells derived from the lymphoma of Abelson murine leukemia virus infected mouse and can differentiate into Oc in the presence of RANKL. As shown by a former SILAC study in Oc, the total proteome of RAW 264.7 Oc is very distinct from that of primary Oc, in particular regarding cytoskeletal organization; unfortunately the data is not available and could not be compared with ours (Ng et al., 2018). Of the 2,073 proteins identified by SILAC during RAW 264.7 osteoclastogenesis (An et al., 2014), there were 1,517 in common with our study, including 93 in our primary Oc protein signature (Table 1). Only 56 of these were found up regulated during RAW264.7 Oc differentiation, even though that study used a $\log_2$ expression ratio cut off at 0.5 less stringent than ours (Table 1, ↗). The other proteins were found down regulated or unchanged during RAW264.7 osteoclastic

differentiation (orange highlight in Table 1, respectively ↘ and =), including known regulators of Oc biology induced during differentiation such as Tensin 3 (Touaitahuata et al., 2016) and CD68/macrosialin (Ashley et al., 2011). Moreover, 52 proteins from our Oc signature were not found in the RAW 264.7 Oc SILAC (red highlight in Table 1, n.f.) including 11 established regulators of Oc differentiation or function (green highlight in Table 1). Thus, our proteomic signature of primary Oc comprises 89 proteins that were not found (52) or were found unchanged (21) or down regulated (16) (Table 1, respectively nf, ↘ and =) during RAW264.7 Oc differentiation, the only global SILAC proteome available so far for Oc (An et al., 2014). They included 15 known actors of Oc biology (green highlight in Table 1) and 36 proteins involved in biological processes activated in Oc: members of v-ATP complex, actors of mitochondrial energy metabolism and mRNA translation. Therefore, the other 38 proteins never studied in Oc could represent proteins with important functions for bone resorption (dark blue highlight Table 1).

Among the 38 proteins of unknown function in Oc, we selected 17 with a variety of functions for a siRNA screening (Fig. 5, bold lines in the dark blue proteins of Table 1). To avoid interference with the early differentiation process, primary Oc cultures were transfected at day 2 of differentiation with a commercial SmartPool of 4 siRNAs (Table 2) and grown for two more days to obtain Oc. We stained actin, tubulin and DNA, acquired mosaic images of entire wells on an automated microscope with a low-magnification objective and full-well images were reconstituted. This screen was performed in triplicate with 3 independent mouse Oc cultures and none of the 17 test siRNAs provoked cytoskeleton organization defects visible at that image resolution; moreover, no significant changes in Oc size were measured (not shown). Remarkably, with 5 siRNAs pools targeting the AKR1C3 homolog Akr1c18, Dmxl1,

Trip11, Vps52 and Wdr7, we observed a high proportion of Oc exhibiting very big and unusual intracellular structures (Fig. 5A-B). These "vacuole-like structures" had a regular circular shape delineated by actin and microtubules and spanned over 10 µm in all directions (Fig. 5B-C). We hypothesized that these structures may emerge from the disturbance of Oc intracellular traffic. In fact, it was shown that the inhibition by YM201636 of lipid kinase PIKfyve, a regulator of the endolysosomal traffic, induces the formation of large endolysosomes in RAW264.7 cells (Hazeki et al., 2013). Similarly, we observed large vesicles in Oc treated with YM201636 positive for the endolysosomal marker CD63/Lamp3, but not delineated by actin (Supp Fig. S5A). By contrast, the vacuole-like structures elicited by the 5 siRNAs in Oc were surrounded by actin but were not delineated by any of the early and late endosomal marker we tested, including CD63 (Fig 5C), suggesting that these structures are not membrane compartments. We could not relate such actin and microtubule-delineated vacuole-like structures to any subcellular compartment reported before.

These results suggest that our Oc signature comprises new regulators of Oc biology, which should be examined in more details to understand their functions.

***Tubb6 regulates Oc cytoskeleton and bone resorption.***

Our SILAC and RNAseq data also revealed changes in the expression of ß-tubulin between Oc, Dc and Mo. Among all α and β tubulin genes, these cells express the same 4 α and 4 β isotypes namely Tubba1a, 1b, 1c and 4a and Tubb2a, 4b, 5 and 6, with Tubb5 and Tubb6 representing more than 80% Tubb reads in the three cell types (Table S2). The protein levels of the 4 α and 4 β isotypes levels were not different between cell types (Table S1), except for Tubb6; this ß tubulin isotype showed 1.375

and 1.256 $log_2$ protein folds as compared to primary Dc and Mo respectively, whereas such increase was not observed during RAW264.7 osteoclastogenesis (Table 1). Interestingly, Tubb6 was reported to have a microtubule destabilizing effect in cycling cells, in contrast with Tubb5 (Bhattacharya and Cabral, 2009; Bhattacharya et al., 2011). As microtubule dynamic instability is important for correct organization of actin and for bone resorption (Biosse Duplan et al., 2014; Guimbal et al., 2019), we explored the biological relevance of increased Tubb6 levels in Oc. Q-PCR analyses confirmed that among ß-tubulin isotypes, Tubb6 expression uniquely increased during primary Oc differentiation (Fig. 6A). We generated 2 siRNAs si1077 and si1373 (Table 1) that specifically target Tubb6; they do not affect the expression of Tubb2a, 4b and 5 RNAs and the global Tubb protein level in Oc (Fig. 6B-C). Whereas Tubb6 siRNAs did not modify the expression of Oc differentiation markers (Fig. S5B-C), they strongly perturbed the organization of the podosome belt, provoking podosomes scattering at cell periphery (Fig. 6D). This was accompanied by a severe modification of microtubule morphology at cell periphery with the appearance of highly buckled microtubules (Fig. 6E). Functionally, Tubb6 knock down resulted in severed reduction in the bone resorption activity of Oc (Fig. 6F). Interestingly, our former analysis of Affymetrix data of human myeloid cells also revealed increased expression of TUBB6 mRNA in Oc derived from human $CD14^+$ peripheral blood monocytes (Gallois et al., 2010; Maurin et al., 2018). Thus, we examined the effect of TUBB6 siRNAs in fully differentiated human Oc from 2 independent donors and found that the number of Oc presenting a normal podosome belt was reduced, consistent with the results we obtained in mouse Oc (Fig. 6G).

These results suggest that the specific ß tubulin isotype repertoire is of functional importance in myeloid cells. In particular that the specific increase in

Tubb6 protein levels that occurs during Oc differentiation is essential for microtubules to ensure correct patterning of Oc podosomes for efficient bone resorption.

## Discussion

We combined SILAC proteomics and RNAseq technologies to homogenous experimental conditions to provide the first comparative global proteomes and transcriptomes of primary mouse Oc and Dc. From the data, we propose a specific proteomic signature for each cell type, which includes proteins of unknown function that represent new candidate regulators of Oc and Dc biology. Using siRNA approach, we explored several of these new candidates in Oc. In particular, we found that Oc, Mo and Dc express the same repertoire of 4α and 4β tubulin isotypes. Within this repertoire, only Tubb6 protein is differentially expressed with higher levels in Oc. We further demonstrate that this increased expression Tubb6 is essential for podosome organization in both mouse and human Oc, and key for the resorption function.

The hematopoietic cells of the monocytic lineage are innate immune cells characterized by a great level of plasticity: mouse bone marrow macrophages and human $CD14^+$ monocytes can differentiate in Dc cells and Oc; moreover, Dc have the capacity to transdifferentiate into Oc (Madel et al., 2019). Still each cell type has a very specific biological function requiring particular cellular processes: Oc are the professional bone resorbing cells that participate in the maintenance of skeleton health whereas Dc are the sentinel antigen-presenting cells that sample their environment for "non-self" entities. Unraveling the molecular pathways underlying the biology of Oc and Dc is key to understand both their physiological and pathological roles. There are only very few proteomic data sets available for Oc; furthermore, because of the difficulty to generate sufficient primary Oc for sample preparation, all were obtained using RAW264.7 cells as Oc precursors (Segeletz and Hoflack, 2016). RAW264.7 is a transformed macrophage-like cell line with osteoclastogenic potential, but this in an M-CSF independent manner; it was reported recently that there were major proteome

discrepancies between primary Oc and Oc derived from RAW 264.7 cells, in particular regarding cytoskeleton regulatory pathways (Ng et al., 2018). Here we developed an experimental approach to prepare primary Mo, Oc and Dc amenable for quantitative SILAC proteomics. Thereby, we provide the first global quantitative proteomic dataset for primary Oc. It is very likely the 145 and 183 proteins we respectively highlighted as Oc and Dc signatures contain new regulators of the biology of each cell type. We compared our primary Oc signature to the only SILAC global proteomics data reported for Oc, which was obtained from RAW264.7 cells (An et al., 2014). Among the 93 proteins of our primary Oc signature also detected in RAW264.7 Oc, not less than 37 proteins were not changed or down-regulated during RAW264.7 osteoclastogenesis; this includes proteins reported to be induced during primary Oc differentiation and essential for bone resorption such as Tensin 3 (Touaitahuata et al., 2016) and CD68/Microsialin (Ashley et al., 2011). This confirmed the potential relevance of the 38 proteins in our primary Oc signature that are of unknown function in Oc yet.

We performed an siRNA screen on 17 randomly picked among these 38 proteins that did not show drastic changes in cell morphology nor major cytoskeleton organization defects of the podosome belt. Interestingly, 5 siRNAs provoked the appearance of large vacuole-like structures in Oc. The 5 target genes have diverse functions: Dmxl1 and Wdr7 are essential vATPase accessory proteins (Merkulova et al., 2015), Trip11 encodes GMAP-210 involved in vesicle tethering to Golgi (Roboti et al., 2015), Vps52 is involved in endosome recycling (Schindler et al., 2015) and Akr1c18 is the mouse homolog of aldoketo-reductase AKR1C3 that converts progesterone (Lanišnik Rižner and Penning, 2019). Such intracellular structures delineated with actin and microtubules but without endosomal membrane marker were

not described before, making it uneasy to hypothesize what molecular mechanism may be perturbed. We found that lipid kinase Pikfyve inhibition could induce very large intracellular structures of similar size in Oc but, as reported in RAW264.7 cells (Hazeki et al., 2013), these were endolysosomal membrane compartments not delineated by actin. More studies are needed on these 38 new potential regulators of Oc biology, which may require stable knock down or knock out models to understand their precise functions.

The Oc signature also contained tubulin ß isotype Tubb6 (Tubulin beta 6 class V). In Oc, Mo and Dc cells, we found that the tubulin repertoire was restricted to the expression of only 4 α and 4 β tubulin genes; they do not express RNA for other tubulin isotypes such as Tubb1 that is needed for proplatelets elongation in megakaryocytes, another myeloid lineage hematopoietic cells (van Dijk et al., 2018). This suggests the existence of a tight transcriptional control of the tubulin repertoire during hematopoiesis, but the mechanisms regulating of the transcription of tubulin genes remains very poorly understood (Gasic and Mitchison, 2019). How different tubulin isotypes affect microtubule dynamics to influence various processes in differentiated cells is an open question. The recent advances in producing recombinant tubulin isoforms started to shed light on the different biochemical properties of tubulin ß isotypes that can influence microtubule dynamics *in vitro* (Roll-Mecak, 2019). Tubb6 has the unusual property to destabilize microtubules in cycling cells whereas it is not the case for Tubb5; this effect appears to rely specifically on the core domain of Tubb6 and not on its tail (Bhattacharya and Cabral, 2009; Bhattacharya et al., 2011). Two aminoacids Ser239 and Ser365 in the core domain are critical for the microtubule destabilizing effect of Tubb6, and they are substituted for Cys in Tubb5. Interestingly, Tubb3 bears Ser239 and Ser365 like in Tubb6 whereas Tubb2b has two Cys like in

Tubb5. Biochemical studies revealed that Tubb3 and Tubb2b have distinct effects *in vitro*: on microtubule dynamics, on their association with microtubule associated proteins (MAP) as well as on their structure (Pamula et al., 2016; Ti et al., 2018). Therefore it is very likely that the level of Tubb6 can influence microtubule intrinsic properties as well as their dynamic behavior and association with MAP in Oc. Indeed, we found that the reduction of Tubb6 in Oc has a strong effect on microtubule and podosome organization, resulting in impaired resorption activity. Contrarily to Tubb5 that is usually a major ß tubulin isotype with Tubb4b, the expression of Tubb6 is low in most tissues (Leandro-García et al., 2010), and the tight control of Tubb6 expression levels appear key to various processes in differentiated cells. In fact, TUBB6 is among the most up-regulated genes in Duchenne muscular dystrophy (DMD) and persistent elevation of Tubb6 levels drives microtubule disorganization in the fibers of muscles in DMD mice (Randazzo et al., 2019). TUBB6 levels also control the execution of pyroptosis by bacteria-infected lymphoblastoid cells (Salinas et al., 2014). We show here that higher amount of Tubb6 in Oc is key for actin organization and the resorption function. Recent reports highlighted the importance of microtubule dynamics and their cross talk with actin to control podosome patterning in Oc and bone resorption (Biosse Duplan et al., 2014; Guimbal et al., 2019; Zalli et al., 2016). Thus, the enrichment of Tubb6 in Oc is very likely to participate in the molecular processes controlling actin and microtubule crosstalk to ensure efficient bone resorption. Whether it functions through affecting intrinsic microtubule dynamics, MAP binding or both remains to be elucidated.

In summary, we designed a homogeneous experimental set up to generate protein and RNA samples of primary Oc and Dc leading to relevant protein and transcript signatures of the two myeloid cell types. In particular, we found that high

levels of ß tubulin isotype Tubb6 is characteristic and functionally relevant in Oc. Further studies on the specific properties of Tubb6 will bring better knowledge about the crosstalk between microtubules and actin cytoskeleton, which remains poorly understood, taking advantage of the unique functional context of bone resorption by Oc. This should be valuable also in the context of osteolytic bone diseases and pave the way for novel strategies against osteoporosis by targeting Oc cytoskeleton.

## Materials and methods.

### *Animals, human samples and ethics statement*

4-week-old C57Bl/6J mice were purchased from Harlan France and maintained in the animal facilities of the CNRS in Montpellier, France. Procedures involving mice were performed in compliance with local animal welfare laws, guidelines and policies, according to the rules of the regional ethical committee. Monocytes from healthy subjects were provided by Etablissement Français du Sang (EFS), Toulouse, France, under contract 21/PLER/TOU/IPBS01/20130042.

### *Production of bone marrow macrophages, osteoclasts and immature dendritic cells for SILAC and RNAseq*

Bone marrow cells were extracted from long bones of C57BL/6J mice 6 to 8 weeks of age as described (Guimbal et al., 2019) and cultured in α-minimal essential medium (α-MEM, Lonza) containing 10% Fetal Bovine Serum (FBS, BioWest), heat inactivated at 56°C for 30 minutes, 2 mM glutamine (Lonza) and 100 U/mL penicillin and streptomycin (Lonza), 3 x $10^7$ cells per 150 mm dishes at 37°C, 5.5% $CO_2$, in a humidified incubation for 24 hours. Non-adherent cells were then collected and used to differentiate the three myeloid cell types and prepare samples for stable isotope labeling by amino acids (SILAC) and RNAseq (Fig. 1A-B). For bone marrow macrophages (Mo) and osteoclasts (Oc), non-adherent cells were then plated 5 x $10^6$ cells per 10-cm plate in the same medium containing 100 ng/ml Macrophage colony-stimulating factor (M-CSF, Miltenyi) for 5 days. Cells were then detached using

Accutase (SIGMA), washed in PBS and resuspended in Roswell Park Memorial Institute (RPMI) medium: SILAC RPMI 1640 (Lonza) supplemented with 10% dialyzed FBS (Life Technologies), 2.4 mM L-Prolin (SIGMA), 2 mM glutamine (Lonza) and 100 U/mL penicillin/streptomycin (Lonza). For Mo RNAseq and SILAC sample preparation, cells were then plated 0.8 x $10^5$ cell per well in 24 well plates in RPMI medium supplemented with 30 ng/ml M-CSF and with the non isotope-labeled (L) amino acid L-enantiomers Lys (0.4 mM) and Arg (0.8 mM) (SIGMA). For Oc RNAseq sample preparation, cells were plated 1 x $10^5$ cell per well in 24 well plates in RPMI medium supplemented with 30 ng/ml M-CSF and 50 ng/ml Receptor Activator of NF-κB Ligand (RANKL, Miltenyi) and with L amino acids as above. For Oc SILAC samples, L amino acids were substituted for the same concentrations of heavy isotope–labeled (H) aminoacids $^{13}C_6$-$^{15}N_2$ L-Lys:2HCl and $^{13}C_6$-$^{15}N_4$ L-Arg (Cambridge Isotope Laboratories). For immature dendritic cells (Dc) RNAseq sample preparation, cells were plated 4x$10^5$ cells per well in 24 well plates in RPMI medium supplemented with 20 ng/ml Granulocyte Macrophage Colony Stimulating Factor (GM-CSF, Miltenyi) and with non L amino acids as above. For Dc SILAC sample preparation, L amino acids were substituted for the same concentrations of intermediate isotope–labeled (M) aminoacids 4,4,5,5-D4 L-Lys:2HCl and $^{13}C_6$ L-Arg (Cambridge Isotope Laboratories). All media were changed every other day for 8 to 10 days. In these conditions, H and M amino acid incorporation in Oc and Dc respectively was over 95% and the Arg to Pro conversion rate was below 0.4%.

***Protein and RNA extraction***

Following differentiation, Oc cultures were incubated with 120 µl per well Accutase (SIGMA), to remove mono-nucleated cells. Then all cultures were rinsed once with PBS and processed for protein or RNA extraction. For SILAC samples, cells were lysed in 8M urea (SIGMA) and 10 mM HEPES (SIGMA), pH 8.0, 12 wells per cell type in a total of 400 µl. Cell lysates were centrifuged at 20,000 x g for 2 minutes; protein concentration was determined using BCA reagent (ThermoFisher), protein concentration was around 25 µg/mL per sample. Lysates were stored at -80°C until SILAC proteomic analysis. For each SILAC analysis, Oc, Dc and Mo protein samples derived from the same mouse; the experiment was done in triplicate with three independent mouse bone marrow extractions.

For RNAseq, total RNA was extracted and purified using RNeasy Mini Kit and QIAshredder spin columns (QIAGEN) according to manufacturer's instructions, 8 wells for Dc, 12 well for Mo and 4 wells for Dc, to obtain around 10 µg of RNA. RNA concentration was measured using a Nanodrop UV-visible spectrophotometer (Thermo Scientific) and RNA quality was assessed using a Bioanalyzer 2100 (Agilent Technologies). Lysates were stored at -80°C until RNAseq analysis. For each RNAseq analysis, Oc, Dc and Mo RNA samples derived from the same mouse, the experiment was done four times with four independent mouse bone marrow extractions.

***RNAseq analyses***

The 12 RNA samples (2 µg) were processed and analyzed in parallel by Fasteris SA (Switzerland), according to the "HiSeq Service Stranded Standard Protocol" (https://support.illumina.com/sequencing/sequencing_instruments/hiseq-3000.html). The stranded mRNA libraries were sequenced by HiSeq 4000 Illumina technology,

generating single reads of 1x 50 bp. Adapter sequences were removed from the obtained 1x 50 bp reads and adapter trimmed reads were used for further analysis. About 30 million raw reads were obtained per sample (from 26,717,590 to 36,916,924), with around 99% of the reads mapping on reference mouse genome GRCm38. Multiple mapping percentages ranged between 23.62 and 32.43% according to sample (Fig. S1C). Sequence mapping (Mus musculus genome GRCm38, from iGenome downloaded on the 2017-07-13), normalization and estimation of transcript abundances (FKPM) were performed using the Tuxedo suite of short read mapping tools (Bowtie v2.0.5, Tophat v2.0.6, Samtools 1.2 and Cufflinks v2.1.1). Differential expression analysis was performed with DESeq2 R package from Bioconductor v2.13. For each comparison by pairs, the mean of the normalized counts obtained for the four replicates within each group of samples was calculated as well as the $\log_2$ fold change. The p, adjusted for multiple testing with the Benjamini-Hochberg procedure, was used to qualify fold changes as significant (padj<0.05).

***Mass spectrometry sample preparation, LC-MS-MS analysis and protein quantification***

Within each of the 3 replicate SILAC experiments, equal amounts of Oc and Mo or Oc and Dc or Dc and Mo proteins were mixed, leading to a total of 9 samples that were processed in parallel. All MS grade reagent were from Thermo Fisher Scientific, grade Optima. For each sample, a total of 10 µg of proteins were digested with 0.5 µg LysC (Wako) in 600 µl of 100 mM triethylammonium bicarbonate for 1 hour at 30°C. Then samples were diluted 3 times in the buffer and 1 µg trypsin (Gold, Promega) was added overnight at 30°C. Peptides were then desalted using OMIX (Agilent) and

analyzed online by nano-flow HPLC-nanoelectrospray ionization using a Qexactive HF mass spectrometer (Thermo Fisher Scientific) coupled to a nano- LC system (U3000-RSLC, Thermo Fisher Scientific). Desalting and preconcentration of samples were performed on-line on a Pepmap® precolumn (0.3 × 10 mm; Thermo Fisher Scientific). A gradient consisting of 0–40% B in A for 120 min (A: 0.1% formic acid, 2% acetonitrile in water, and B: 0.1% formic acid in 80% acetonitrile) at 300 nL/min, was used to elute peptides from the capillary reverse-phase column (0.075 × 500 mm, Pepmap®, Thermo Fisher Scientific). Data were acquired using the Xcalibur 4.0 software. A cycle of one full-scan mass spectrum (375–1,500m/z) at a resolution of 60,000 (at 200 m/z), followed by 12 data-dependent MS/MS spectra (at a resolution of 30,000, isolation window 1.2 m/z) was repeated continuously throughout the nanoLC separation.

Raw data analysis was performed using the MaxQuant software (version 1.5.5.1) with standard settings. Used database consist of mouse entries from UniProt (reference proteome UniProt 2016_11), 250 contaminants (MaxQuant contaminant database) and corresponding reverse entries. Each protein identified was associated to the corresponding gene in Mus musculus genome GRCm38. Relative proteins quantifications were calculated on the median SILAC ratios to determine $\log_2$ fold changes. In each comparison, proteins with $|\log_2$ abundance ratio$| \geq 0.75$ were considered differentially abundant.

***Other bioinformatic analyses***

Principal component analyses of both proteomic and transcriptomic results were made using R. software. For RNAseq, the hierarchical clustering analysis was

performed in MeV tool v4.9 (Saeed et al., 2003) using the four normalized expression counts for each cell type. Before analysis, values were normalized by rows using the software. An average linkage algorithm from a distance matrix calculated with the Pearson correlation coefficient was employed to make the analysis. Comparison between RNAseq and SILAC results and linear regressions were made using Graphpad Prism 5 software. GO term enrichment analyses were performed using Panther software (http://pantherdb.org/). The total lists of proteins and genes identified in this study were used as references. UniProtIDs and Ensembl IDs were employed as input type IDs for proteomic and transcriptomic results respectively. GO terms with p-value $< 0.05$ were considered significantly enriched. Histograms of enriched or diminished GO terms were represented using Graphpad Prism 5 software. Protein-Protein Interactions (PPIs) were determined using the Search Tool for Retrieval of Interacting Genes/Proteins (STRING) software v10.5 (https://string-db.org/) (Szklarczyk et al., 2015). Only interactions based on experimental source with interaction score $\geq 0.7$ were considered. PPIs networks were then represented using Cytoscape v3.6.1 (http://www.cytoscape.org/index.html) (Shannon et al., 2003).

***Mouse Oc cultures for siRNA treatment and immunofluorescence.***

Mouse primary Oc were differentiated from bone marrow cells of 6-8-week-old C57BL/6J mice as described (Guimbal et al., 2019). At day 2 of differentiation, siRNAs were transfected with siImporter in OptiMEM medium (Life Technologies) containing 30 ng/mL M- CSF and 50 ng/mL RANKL as described (Touaitahuata et al., 2016) using 100 nM siRNA: either Dharmacon siGenome Smartpools or custom oligonucleotides from Eurogentec (Table 2). After 3 hours, medium was replaced with

α-MEM medium containing 30 ng/mL M- CSF and 50 ng/mL RANKL and changed every other day during 3 to 4 days, until Oc differentiate. For Pikfyve inhibition, Oc were treated for 1 hour with 1 µM YM201636 (Cayman) in 0.005 % DMSO. Oc were then fixed in 3.2% paraformaldehyde and 10 µM Taxol (SIGMA) in PHEM (Pipes 60 mM, Hepes 25 mM, EGTA 10 mM, MgSO4 4 mM, pH 6.9) for 20 min. For tubulin detection, cells were permeabilized for 1 min with 0.1% Triton X-100 in PBS and saturated with blocking buffer (1% BSA in PBS) before incubation for one hour with anti-α-Tubulin (T5168, SIGMA) 1:2000 in PBS containing 1% BSA. For CD63 (LAMP-3), cells were permeabilized for 2 min with 0.1% Saponin in PBS and saturated with blocking buffer before incubation for one hour with antibody R5G2 (MBL Life Science) 1:200 in PBS containing 1% BSA. Then cells were incubated for one hour in Alexa-conjugated secondary antibodies and/or F-actin marker Alexa-conjugated Phalloidin (Life Technologies) or Rhodamin-labeled Phalloidin (SIGMA), all used 1:1000 in PBS containing 1% BSA containing bisbenzimide Hoechst dye (Sigma) stain DNA.

For siRNA screening, images were acquired at low resolution directly in the 24-well plates with an automated ArrayscanVTi microscope (Thermo) equipped with a 10X EC Plan Neofluar 0.3NA objective as described (Maurin et al., 2018). For confocal imaging, samples were mounted in Citifluor mouting medium (Biovalley) and images were acquired with an SP5 confocal microscope equipped with Leica LAS-AF software with objectives 40X HCX Plan Apo CS 1.3 NA oil or a 63X HCX Plan Apo CS 1.4 NA oil (Leica), or a Zeiss Axioimager Z2 microscope equipped with MetaMorph 7.6.6 Software (Molecular Devices) with objectives 40X EC Plan Neofluar 1.3 NA oil or 63X Plan Apochromat 1.4 NA oil (Zeiss). For Airyscan confocal, imaging was performed with a 63x Plan Apo 1.4NA of a Zeiss LSM880

confocal microscope equipped with an Airyscan detector (32 GaAsp detector) in super resolution mode; Alexa 488 was exited at 488nm with argon laser and Alexa 647 at 633nm with helium/neon laser; Airyscan analysis was made using Zen software with default settings.

***Human Oc cultures for siRNA treatment and immunofluorescence***

For differentiation to human Oc, monocytes purified by $CD14^+$ purification kit (Miltenyi) were seeded on slides in 24-well plates at a density of $5.10^5$ cells per well in RPMI supplemented with 10% FBS (SIGMA), M-CSF (50 ng/mL) and RANKL (30 ng/mL). The medium was then replaced every 3 days with medium containing M-CSF (25 ng/mL) and RANKL (100 ng/mL) (Miltenyi) until Oc differentiation. Targets silencing was performed at day 5 using reverse transfection protocol as previously described (Troegeler et al., 2014). Shortly, cells were transfected with 200 nM of ON-TARGETplus SMARTpool siRNA targeting TUBB6 (Table 2) or the ON-TARGETplus Non-targeting control pool (Dharmacon) using HiPerfect transfection system (Qiagen) in RPMI. Four hours post-transfection, cells were incubated for 24 hours in RPMI-1640 medium, 10% FBS, 20 ng/ml of M-CSF and RANKL (100 ng/mL). After 7 additional days, cells were fixed with PFA 3.7%, Sucrose 30 mM in PBS. After permeabilization with Triton X-100 0,3%, cells were saturated with blocking buffer, washed and incubated with Alexa Fluor 555 Phalloidin (33 mM, Thermo Fisher Scientific) and DAPI (500 ng/mL, Sigma Aldrich) in blocking buffer for 1 hour. Coverslips were mounted with Fluorescence Mounting Medium (Dako). Imaging was performed with a SP5 confocal microscope as above.

***Image quantification, Oc activity assays, Q-PCR and western blot***

The podosome belt status of Oc was determined considering that the podosome belt was abnormal when, in over half of Oc periphery, actin staining was fragmented and/or weak and/or thin and/or absent and/or that podosomes were scattered as described before (Maurin et al., 2018). Total RNA and protein extractions, real time Q-PCR and western blots were performed as reported previously (Maurin et al., 2018) using the primers described in Table 2, primary antibodies against pan beta tubulin (sc-398937 1:1000, Santa Cruz) and Gapdh (#2118 1:10,000, Cell Signalling) and horseradish peroxidase-conjugated secondary antibodies 1:10,000 anti-mouse NA931V or anti-rabbit NA934V (GE Healthcare). Mineral dissolution activity of Oc was measured as described (Maurin et al., 2018). Briefly, at day 3 of differentiation (24 h after siRNA transfection), Oc were detached with Accutase (Sigma) for 5–10 min at 37 °C and seeded for 3 days onto inorganic crystalline calcium phosphate (CaP)-coated multiwells (Osteo Assay Surface, Corning), 8 wells per siRNA. For each siRNA, four wells were then stained for Tartrate Resistant Acid Phosphatase (TRAP) activity to count Oc and four wells stained with Von Kossa to measure CaP dissolution as described (Brazier et al., 2009) and imaged with a Nikon SMZ1000 stereomicroscope equipped with a Nikon DXM 1200F CCD camera. Quantification of resorbed areas per wells was done with ImageJ 1.51w software. In each experiment, Oc specific activity was expressed as the average area resorbed in the 4 wells stained with von Kossa normalized by the average number of the Oc in the 4 wells stained with TRAP. Statistical analyses were performed with GraphPad Prism 5.0. All imaging was performed at the Montpellier Ressources Imagerie (MRI) imaging facility (www.mri.cnrs.fr).

**Acknowledgements**

We acknowledge the imaging facility MRI, member of the national infrastructure France-BioImaging supported by the French National Research Agency (ANR-10-INBS-04, "Investments for the future"). We are very grateful to Frank Comunale, Christelle Dantec, Philippe Fort and Peggy Raynaud for helpful advice and discussions during transcriptomic analysis and for reagent sharing.

**Competing interests**

The authors have declared no conflict of interest.

**Funding**

This study was supported by the French Centre National de la Recherche Scientifique (CNRS), Montpellier University and grants from the French Fondation pour la Recherche Médicale (Grant # DEQ20160334933), GEFLUC Languedoc Roussillon (grant #A.P. 2015) and Société Française de Rhumatologie (grant # 2676 Subvention 2014) to A.B. and a grant from the Fondation ARC (grant # PDF2016-1205179) to P.M.

## References

**An, E., Narayanan, M., Manes, N. P. and Nita-Lazar, A.** (2014). Characterization of functional reprogramming during osteoclast development using quantitative proteomics and mRNA profiling. *Mol Cell Proteomics* **13**, 2687–704.

**Ashley, J. W., Shi, Z., Zhao, H., Li, X., Kesterson, R. A. and Feng, X.** (2011). Genetic ablation of CD68 results in mice with increased bone and dysfunctional osteoclasts. *PloS One* **6**, e25838.

**Baranov, M., Ter Beest, M., Reinieren-Beeren, I., Cambi, A., Figdor, C. G. and van den Bogaart, G.** (2014). Podosomes of dendritic cells facilitate antigen sampling. *J. Cell Sci.* **127**, 1052–1064.

**Bhattacharya, R. and Cabral, F.** (2009). Molecular basis for class V beta-tubulin effects on microtubule assembly and paclitaxel resistance. *J. Biol. Chem.* **284**, 13023–13032.

**Bhattacharya, R., Yang, H. and Cabral, F.** (2011). Class V β-tubulin alters dynamic instability and stimulates microtubule detachment from centrosomes. *Mol. Biol. Cell* **22**, 1025–1034.

**Biosse Duplan, M., Zalli, D., Stephens, S., Zenger, S., Neff, L., Oelkers, J. M., Lai, F. P., Horne, W., Rottner, K. and Baron, R.** (2014). Microtubule dynamic instability controls podosome patterning in osteoclasts through EB1, cortactin, and Src. *Mol Cell Biol* **34**, 16–29.

**Brazier, H., Pawlak, G., Vives, V. and Blangy, A.** (2009). The Rho GTPase Wrch1 regulates osteoclast precursor adhesion and migration. *Int. J. Biochem. Cell Biol.* **41**, 1391–1401.

**Cappariello, A., Maurizi, A., Veeriah, V. and Teti, A.** (2014). The Great Beauty of the osteoclast. *Arch. Biochem. Biophys.* **558**, 70–78.

**Compston, J. E., McClung, M. R. and Leslie, W. D.** (2019). Osteoporosis. *Lancet Lond. Engl.* **393**, 364–376.

**Drake, M. T., Clarke, B. L., Oursler, M. J. and Khosla, S.** (2017). Cathepsin K Inhibitors for Osteoporosis: Biology, Potential Clinical Utility, and Lessons Learned. *Endocr. Rev.* **38**, 325–350.

**Gallois, A., Lachuer, J., Yvert, G., Wierinckx, A., Brunet, F., Rabourdin-Combe, C., Delprat, C., Jurdic, P. and Mazzorana, M.** (2010). Genome-wide expression analyses establish dendritic cells as a new osteoclast precursor able to generate bone-resorbing cells more efficiently than monocytes. *J Bone Min. Res* **25**, 661–72.

**Gasic, I. and Mitchison, T. J.** (2019). Autoregulation and repair in microtubule homeostasis. *Curr. Opin. Cell Biol.* **56**, 80–87.

**Georgess, D., Machuca-Gayet, I., Blangy, A. and Jurdic, P.** (2014a). Podosome organization drives osteoclast-mediated bone resorption. *Cell Adhes. Migr.* **8**, 191–204.

**Georgess, D., Mazzorana, M., Terrado, J., Delprat, C., Chamot, C., Guasch, R. M., Perez-Roger, I., Jurdic, P. and Machuca-Gayet, I.** (2014b). Comparative transcriptomics reveals RhoE as a novel regulator of actin dynamics in bone-resorbing osteoclasts. *Mol Biol Cell* **25**, 380–96.

**Ghazalpour, A., Bennett, B., Petyuk, V. A., Orozco, L., Hagopian, R., Mungrue, I. N., Farber, C. R., Sinsheimer, J., Kang, H. M., Furlotte, N., et al.** (2011). Comparative analysis of proteome and transcriptome variation in mouse. *PLoS Genet.* **7**, e1001393.

**Guimbal, S., Morel, A., Guérit, D., Chardon, M., Blangy, A. and Vives, V.** (2019). Dock5 is a new regulator of microtubule dynamic instability in osteoclasts. *Biol. Cell* **https://doi.org/10.1111/boc.201900014**,.

**Hazeki, K., Uehara, M., Nigorikawa, K. and Hazeki, O.** (2013). PIKfyve regulates the endosomal localization of CpG oligodeoxynucleotides to elicit TLR9-dependent cellular responses. *PloS One* **8**, e73894.

**Hiruma, Y., Tsuda, E., Maeda, N., Okada, A., Kabasawa, N., Miyamoto, M., Hattori, H. and Fukuda, C.** (2013). Impaired osteoclast differentiation and function and mild osteopetrosis development in Siglec-15-deficient mice. *Bone* **53**, 87–93.

**Homan, E. P., Rauch, F., Grafe, I., Lietman, C., Doll, J. A., Dawson, B., Bertin, T., Napierala, D., Morello, R., Gibbs, R., et al.** (2011). Mutations in SERPINF1 cause osteogenesis imperfecta type VI. *J. Bone Miner. Res. Off. J. Am. Soc. Bone Miner. Res.* **26**, 2798–2803.

**Humphrey, M. B., Daws, M. R., Spusta, S. C., Niemi, E. C., Torchia, J. A., Lanier, L. L., Seaman, W. E. and Nakamura, M. C.** (2006). TREM2, a DAP12-associated receptor, regulates osteoclast differentiation and function. *J. Bone Miner. Res. Off. J. Am. Soc. Bone Miner. Res.* **21**, 237–245.

**Khosla, S. and Hofbauer, L. C.** (2017). Osteoporosis treatment: recent developments and ongoing challenges. *Lancet Diabetes Endocrinol.* **5**, 898–907.

**Lanišnik Rižner, T. and Penning, T. M.** (2019). Aldo-keto reductase 1C3 - assessment as a new target for the treatment of endometriosis. *Pharmacol. Res.* 104446.

**Leandro-García, L. J., Leskelä, S., Landa, I., Montero-Conde, C., López-Jiménez, E., Letón, R., Cascón, A., Robledo, M. and Rodríguez-Antona, C.** (2010). Tumoral and tissue-specific expression of the major human beta-tubulin isotypes. *Cytoskelet. Hoboken NJ* **67**, 214–223.

**Lemma, S., Sboarina, M., Porporato, P. E., Zini, N., Sonveaux, P., Di Pompo, G., Baldini, N. and Avnet, S.** (2016). Energy metabolism in osteoclast formation and

activity. *Int. J. Biochem. Cell Biol.* **79**, 168–180.

**Lu, B., Jiao, Y., Wang, Y., Dong, J., Wei, M., Cui, B., Sun, Y., Wang, L., Zhang, B., Chen, Z., et al.** (2017). A FKBP5 mutation is associated with Paget's disease of bone and enhances osteoclastogenesis. *Exp. Mol. Med.* **49**, e336.

**Madel, M.-B., Ibáñez, L., Wakkach, A., de Vries, T. J., Teti, A., Apparailly, F. and Blin-Wakkach, C.** (2019). Immune Function and Diversity of Osteoclasts in Normal and Pathological Conditions. *Front. Immunol.* **10**, 1408.

**Maruyama, K., Kawagoe, T., Kondo, T., Akira, S. and Takeuchi, O.** (2012). TRAF family member-associated NF-κB activator (TANK) is a negative regulator of osteoclastogenesis and bone formation. *J. Biol. Chem.* **287**, 29114–29124.

**Maurin, J., Morel, A., Hassen-Khodja, C., Vives, V., Jurdic, P., Machuca-Gayet, I. and Blangy, A.** (2018). Combined strategy of siRNA and osteoclast actin cytoskeleton automated imaging to identify novel regulators of bone resorption shows a non-mitotic function for anillin. *Eur. J. Cell Biol.* **97**, 568–579.

**Merkulova, M., Păunescu, T. G., Azroyan, A., Marshansky, V., Breton, S. and Brown, D.** (2015). Mapping the H(+) (V)-ATPase interactome: identification of proteins involved in trafficking, folding, assembly and phosphorylation. *Sci. Rep.* **5**, 14827.

**Nagai, Y., Osawa, K., Fukushima, H., Tamura, Y., Aoki, K., Ohya, K., Yasuda, H., Hikiji, H., Takahashi, M., Seta, Y., et al.** (2013). p130Cas, Crk-associated substrate, plays important roles in osteoclastic bone resorption. *J. Bone Miner. Res. Off. J. Am. Soc. Bone Miner. Res.* **28**, 2449–2462.

**Narahara, S., Sakai, E., Kadowaki, T., Yamaguchi, Y., Narahara, H., Okamoto, K., Asahina, I. and Tsukuba, T.** (2019). KBTBD11, a novel BTB-Kelch protein, is a negative regulator of osteoclastogenesis through controlling Cullin3-mediated ubiquitination of NFATc1. *Sci. Rep.* **9**, 3523.

**Ng, A. Y., Tu, C., Shen, S., Xu, D., Oursler, M. J., Qu, J. and Yang, S.** (2018). Comparative Characterization of Osteoclasts Derived From Murine Bone Marrow Macrophages and RAW 264.7 Cells Using Quantitative Proteomics. *JBMR Plus* **2**, 328–340.

**Ochotny, N., Flenniken, A. M., Owen, C., Voronov, I., Zirngibl, R. A., Osborne, L. R., Henderson, J. E., Adamson, S. L., Rossant, J., Manolson, M. F., et al.** (2011). The V-ATPase a3 subunit mutation R740S is dominant negative and results in osteopetrosis in mice. *J. Bone Miner. Res. Off. J. Am. Soc. Bone Miner. Res.* **26**, 1484–1493.

**Pamula, M. C., Ti, S.-C. and Kapoor, T. M.** (2016). The structured core of human β tubulin confers isotype-specific polymerization properties. *J. Cell Biol.* **213**, 425–433.

**Randazzo, D., Khalique, U., Belanto, J. J., Kenea, A., Talsness, D. M., Olthoff, J. T., Tran, M. D., Zaal, K. J., Pak, K., Pinal-Fernandez, I., et al.** (2019). Persistent

upregulation of the β-tubulin tubb6, linked to muscle regeneration, is a source of microtubule disorganization in dystrophic muscle. *Hum. Mol. Genet.* **28**, 1117–1135.

**Real, E., Kaiser, A., Raposo, G., Amara, A., Nardin, A., Trautmann, A. and Donnadieu, E.** (2004). Immature dendritic cells (DCs) use chemokines and intercellular adhesion molecule (ICAM)-1, but not DC-specific ICAM-3-grabbing nonintegrin, to stimulate CD4+ T cells in the absence of exogenous antigen. *J. Immunol. Baltim. Md 1950* **173**, 50–60.

**Roboti, P., Sato, K. and Lowe, M.** (2015). The golgin GMAP-210 is required for efficient membrane trafficking in the early secretory pathway. *J. Cell Sci.* **128**, 1595–1606.

**Roll-Mecak, A.** (2019). How cells exploit tubulin diversity to build functional cellular microtubule mosaics. *Curr. Opin. Cell Biol.* **56**, 102–108.

**Sabado, R. L., Balan, S. and Bhardwaj, N.** (2017). Dendritic cell-based immunotherapy. *Cell Res.* **27**, 74–95.

**Saeed, A. I., Sharov, V., White, J., Li, J., Liang, W., Bhagabati, N., Braisted, J., Klapa, M., Currier, T., Thiagarajan, M., et al.** (2003). TM4: a free, open-source system for microarray data management and analysis. *BioTechniques* **34**, 374–378.

**Salinas, R. E., Ogohara, C., Thomas, M. I., Shukla, K. P., Miller, S. I. and Ko, D. C.** (2014). A cellular genome-wide association study reveals human variation in microtubule stability and a role in inflammatory cell death. *Mol. Biol. Cell* **25**, 76–86.

**Schindler, C., Chen, Y., Pu, J., Guo, X. and Bonifacino, J. S.** (2015). EARP is a multisubunit tethering complex involved in endocytic recycling. *Nat. Cell Biol.* **17**, 639–650.

**Segeletz, S. and Hoflack, B.** (2016). Proteomic approaches to study osteoclast biology. *Proteomics* **16**, 2545–2556.

**Shannon, P., Markiel, A., Ozier, O., Baliga, N. S., Wang, J. T., Ramage, D., Amin, N., Schwikowski, B. and Ideker, T.** (2003). Cytoscape: a software environment for integrated models of biomolecular interaction networks. *Genome Res.* **13**, 2498–2504.

**Szklarczyk, D., Franceschini, A., Wyder, S., Forslund, K., Heller, D., Huerta-Cepas, J., Simonovic, M., Roth, A., Santos, A., Tsafou, K. P., et al.** (2015). STRING v10: protein-protein interaction networks, integrated over the tree of life. *Nucleic Acids Res.* **43**, D447-452.

**Ti, S.-C., Alushin, G. M. and Kapoor, T. M.** (2018). Human β-Tubulin Isotypes Can Regulate Microtubule Protofilament Number and Stability. *Dev. Cell* **47**, 175-190.e5.

**Tiberio, L., Del Prete, A., Schioppa, T., Sozio, F., Bosisio, D. and Sozzani, S.** (2018). Chemokine and chemotactic signals in dendritic cell migration. *Cell. Mol. Immunol.* **15**, 346–352.

**Touaitahuata, H., Blangy, A. and Vives, V.** (2014). Modulation of osteoclast differentiation and bone resorption by Rho GTPases. *Small GTPases* **5**, e28119.

**Touaitahuata, H., Morel, A., Urbach, S., Mateos-Langerak, J., de Rossi, S. and Blangy, A.** (2016). Tensin 3 is a new partner of Dock5 that controls osteoclast podosome organization and activity. *J. Cell Sci.* **129**, 3449–3461.

**Troegeler, A., Lastrucci, C., Duval, C., Tanne, A., Cougoule, C., Maridonneau-Parini, I., Neyrolles, O. and Lugo-Villarino, G.** (2014). An efficient siRNA-mediated gene silencing in primary human monocytes, dendritic cells and macrophages. *Immunol Cell Biol* **92**, 699–708.

**Turner, A. G., Tjahyono, F., Chiu, W. S. M., Skinner, J., Sawyer, R., Moore, A. J., Morris, H. A., Findlay, D. M., Zajac, J. D. and Davey, R. A.** (2011). The role of the calcitonin receptor in protecting against induced hypercalcemia is mediated via its actions in osteoclasts to inhibit bone resorption. *Bone* **48**, 354–361.

**van Dijk, J., Bompard, G., Cau, J., Kunishima, S., Rabeharivelo, G., Mateos-Langerak, J., Cazevieille, C., Cavelier, P., Boizet-Bonhoure, B., Delsert, C., et al.** (2018). Microtubule polyglutamylation and acetylation drive microtubule dynamics critical for platelet formation. *BMC Biol.* **16**, 116.

**Vives, V., Laurin, M., Cres, G., Larrousse, P., Morichaud, Z., Noel, D., Côté, J.-F. and Blangy, A.** (2011). The Rac1 exchange factor Dock5 is essential for bone resorption by osteoclasts. *J. Bone Miner. Res. Off. J. Am. Soc. Bone Miner. Res.* **26**, 1099–1110.

**Vives, V., Cres, G., Richard, C., Busson, M., Ferrandez, Y., Planson, A.-G., Zeghouf, M., Cherfils, J., Malaval, L. and Blangy, A.** (2015). Pharmacological inhibition of Dock5 prevents osteolysis by affecting osteoclast podosome organization while preserving bone formation. *Nat. Commun.* **6**, 6218.

**Wculek, S. K., Cueto, F. J., Mujal, A. M., Melero, I., Krummel, M. F. and Sancho, D.** (2019). Dendritic cells in cancer immunology and immunotherapy. *Nat. Rev. Immunol.*

**Zalli, D., Neff, L., Nagano, K., Shin, N. Y., Witke, W., Gori, F. and Baron, R.** (2016). The Actin-Binding Protein Cofilin and Its Interaction With Cortactin Are Required for Podosome Patterning in Osteoclasts and Bone Resorption In Vivo and In Vitro. *J. Bone Miner. Res.* **31**, 1701–1712.

# Tables

## Table 1: Proteins of the primary osteoclast signature

See also Excel file

| Gene Symbol | Description | UniProt ID | Ensembl Gene | SILAC | RNAseq | SILAC | RNAseq | SILAC |
|---|---|---|---|---|---|---|---|---|
| **Known regulators of Ocs** | | | | | | | | |
| Acp5 | Tartrate-resistant acid phosphatase type 5 | Q05117 | ENSMUSG00000001348 | 7.408 | 4.042 | 6.859 | 8.356 | ↗ |
| Atp6v0d2 | V-type proton ATPase subunit d 2 | Q80SY3 | ENSMUSG00000028238 | 2.295 | n.s. | 2.018 | 2.480 | ↗ |
| Atp6v1c1 | V-type proton ATPase subunit C 1 | Q9Z1G3 | ENSMUSG00000022295 | 2.112 | 1.087 | 1.038 | 0.540 | ↗ |
| Atp6v1h | V-type proton ATPase subunit H | Q8BVE3 | ENSMUSG00000033793 | 1.958 | 0.808 | 1.479 | 0.625 | ↗ |
| Ca2 | Carbonic anhydrase 2 | P00920 | ENSMUSG00000027562 | 1.150 | -0.762 | 2.439 | 6.759 | n.f. |
| Ccr1 | C-C chemokine receptor type 1 | P51675 | ENSMUSG00000025804 | 1.213 | -1.427 | absent in Mo | 2.704 | n.f. |
| Cd44 | CD44 antigen | P15379 | ENSMUSG00000005087 | 1.274 | 0.537 | 1.269 | 0.633 | ↗ |
| Cd68 | Macrosialin | P31996 | ENSMUSG00000018774 | 1.884 | 1.304 | 1.358 | n.s. | = |
| Ckb | Creatine kinase B-type | Q04447 | ENSMUSG00000001270 | 3.828 | 2.882 | 2.252 | 1.891 | ↗ |
| Cstb | Cystatin-B | Q62426 | ENSMUSG00000005054 | 1.275 | 0.624 | 0.750 | 0.914 | ↗ |
| Ctsk | Cathepsin K | P55097 | ENSMUSG00000028111 | 2.805 | 5.830 | 3.175 | 9.204 | ↗ |
| Dock5 | Dedicator of cytokinesis protein 5 | B2RY04 | ENSMUSG00000044447 | 1.570 | 1.342 | 1.803 | 1.770 | ↗ |
| Git1 | ARF GTPase-activating protein GIT1 | Q68FF6 | ENSMUSG00000011877 | 0.961 | 0.882 | 1.272 | 0.832 | ↗ |
| Kbtbd11 | Kelch repeat and BTB domain-containing protein 11 | Q8BNW9 | ENSMUSG00000055675 | 3.157 | 2.642 | 1.503 | 5.718 | n.f. |
| Ldhb | L-lactate dehydrogenase B chain | P16125 | ENSMUSG00000030246 | 2.436 | n.s. | 2.685 | 2.208 | n.f. |
| Mdh1 | Malate dehydrogenase, cytoplasmic | P14152 | ENSMUSG00000020321 | 1.491 | 0.708 | 0.900 | 0.625 | ↗ |
| Myo1d | Unconventional myosin-Id | Q5SYD0 | ENSMUSG00000035441 | 1.702 | 3.296 | 2.342 | 3.088 | n.f. |
| Prmt5 | Protein arginine N-methyltransferase 5 | Q8CIG8 | ENSMUSG00000023110 | absent in Dc | 0.764 | 1.177 | 0.474 | = |
| Pstpip1 | Proline-serine-threonine phosphatase-interacting protein 1 | P97814 | ENSMUSG00000032322 | 1.445 | 0.986 | 0.990 | 1.035 | ↗ |
| Rabggtb | Geranylgeranyl transferase type-2 subunit beta | P53612 | ENSMUSG00000038975 | 1.899 | n.s. | 1.067 | 0.327 | n.f. |
| Scin | Adseverin | Q60604 | ENSMUSG00000002565 | 1.715 | 2.490 | 2.374 | 7.229 | n.f. |
| Snx10 | Sorting nexin-10 | Q9CWT3 | ENSMUSG00000038301 | 1.313 | 1.240 | absent in Mo | 1.386 | n.f. |
| Tank | TRAF family member-associated NF-kappa-B activator | P70347 | ENSMUSG00000064289 | absent in Dc | n.s. | 1.746 | 0.978 | n.f. |
| Tcirg1 | V-type proton ATPase subunit a | Q9JHF5 | ENSMUSG00000001750 | 2.374 | 0.725 | 2.324 | 1.015 | n.f. |
| Tfrc | Transferrin receptor protein 1 | Q62351 | ENSMUSG00000022797 | 1.259 | 2.498 | 0.859 | 2.386 | = |
| Tns3 | Tensin-3 | Q5SSZ5 | ENSMUSG00000020422 | 1.602 | 2.647 | 0.925 | n.s. | = |
| Trem2 | Triggering receptor expressed on myeloid cells 2 | Q99NH8 | ENSMUSG00000023992 | 1.798 | 1.224 | absent in Mo | -0.778 | n.f. |
| **vATPase subunits** | | | | | | | | |
| Atp6v1a | V-type proton ATPase catalytic subunit A | P50516 | ENSMUSG00000052459 | 2.147 | 1.621 | 1.373 | n.s. | ↗ |
| Atp6v1b2 | V-type proton ATPase subunit B, brain isoform | P62814 | ENSMUSG00000006273 | 2.119 | n.s. | 1.381 | 1.057 | ↗ |
| Atp6v1d | V-type proton ATPase subunit D | P57746 | ENSMUSG00000021114 | 1.911 | 0.790 | 1.818 | 0.847 | ↗ |
| Atp6v1e1 | V-type proton ATPase subunit E 1 | P50518 | ENSMUSG00000019210 | 2.007 | n.s. | 1.142 | 0.480 | ↗ |
| Atp6v1f | V-type proton ATPase subunit F | Q9D1K2 | ENSMUSG00000004285 | 1.845 | n.s. | 1.264 | n.s. | n.f. |
| Atp6v1g1 | V-type proton ATPase subunit G 1 | Q9CR51 | ENSMUSG00000039105 | 2.101 | 0.934 | 1.082 | 0.811 | n.f. |
| **Energy metabolism** | | | | | | | | |
| *Mitochondria* | | | | | | | | |
| Acaa2 | 3-ketoacyl-CoA thiolase, mitochondrial | Q8BWT1 | ENSMUSG00000036880 | 1.639 | 0.493 | 1.529 | 1.149 | ↗ |
| Acadvl | Very long-chain specific acyl-CoA dehydrogenase, mitochondrial | P50544 | ENSMUSG00000018574 | 1.313 | 0.402 | 0.778 | 0.302 | ↗ |
| Acat1 | Acetyl-CoA acetyltransferase, mitochondrial | Q8QZT1 | ENSMUSG00000032047 | 1.174 | n.s. | 0.887 | 0.552 | ↗ |
| Aco2 | Aconitate hydratase, mitochondrial | Q99KI0 | ENSMUSG00000022477 | 1.622 | 0.465 | 1.340 | 0.942 | ↗ |
| Aldh4a1 | Delta-1-pyrroline-5-carboxylate dehydrogenase, mitochondrial | Q8CHT0 | ENSMUSG00000028737 | 0.915 | n.s. | 1.136 | 0.456 | n.f. |
| Atp5a1 | ATP synthase subunit alpha, mitochondrial | Q03265 | ENSMUSG00000025428 | 0.818 | n.s. | 0.934 | 0.600 | = |
| Atp5b | ATP synthase subunit beta, mitochondrial | P56480 | ENSMUSG00000025393 | 0.761 | n.s. | 1.025 | 0.896 | ↗ |
| Atp5d | ATP synthase subunit delta, mitochondrial | Q9D3D9 | ENSMUSG00000003072 | 0.835 | n.s. | 0.866 | 0.750 | = |
| Atp5h | ATP synthase subunit d, mitochondrial | Q9DCX2 | ENSMUSG00000034566 | 0.759 | -0.249 | 1.007 | 0.291 | ↗ |
| Atp5o | ATP synthase subunit O, mitochondrial | Q9DB20 | ENSMUSG00000022956 | 0.952 | n.s. | 0.778 | 0.753 | = |
| Cisd1 | CDGSH iron-sulfur domain-containing protein 1 | Q91WS0 | ENSMUSG00000037710 | 0.880 | n.s. | 1.056 | 0.713 | n.f. |
| Cox4i1 | Cytochrome c oxidase subunit 4 isoform 1, mitochondrial | P19783 | ENSMUSG00000031818 | 1.514 | n.s. | 1.059 | n.s. | ↗ |
| Cox6a1 | Cytochrome c oxidase subunit 6A1, mitochondrial | P43024 | ENSMUSG00000041697 | 0.976 | n.s. | 0.945 | 0.603 | n.f. |
| Cox7a2 | Cytochrome c oxidase subunit 7A2, mitochondrial | P48771 | ENSMUSG00000032330 | 0.970 | n.s. | 1.126 | 0.631 | n.f. |
| Cs | Citrate synthase, mitochondrial | Q9CZU6 | ENSMUSG00000005683 | 1.029 | n.s. | 1.055 | 0.869 | ↗ |
| Cyc1 | Cytochrome c1, heme protein, mitochondrial | Q9D0M3 | ENSMUSG00000022551 | 1.092 | 0.345 | 1.078 | 1.221 | ↗ |
| Dlst | Dihydrolipoyllysine-residue succinyltransferase component of 2-oxoglutarate dehydrogenase complex, mitochondrial | Q9D2G2 | ENSMUSG00000004789 | 0.966 | n.s. | 1.297 | 0.746 | ↗ |
| Etfdh | Electron transfer flavoprotein-ubiquinone oxidoreductase, mitochondrial | Q921G7 | ENSMUSG00000027809 | 2.002 | 0.500 | 1.221 | 0.703 | ↗ |
| Hagh | Hydroxyacylglutathione hydrolase, mitochondrial | Q99KB8 | ENSMUSG00000024158 | 2.200 | 1.466 | 1.365 | 1.343 | ↗ |
| Hsd17b10 | 3-hydroxyacyl-CoA dehydrogenase type-2 | O08756 | ENSMUSG00000025260 | 1.290 | 1.203 | 1.594 | 1.233 | ↗ |
| Idh3a | Isocitrate dehydrogenase [NAD] subunit alpha, mitochondrial | Q9D6R2 | ENSMUSG00000032279 | 1.197 | 0.695 | 1.649 | 1.341 | ↗ |
| Idh3b | Isocitrate dehydrogenase [NAD] subunit, mitochondrial | Q91VA7 | ENSMUSG00000027406 | 1.063 | 0.374 | 1.150 | 0.418 | n.f. |
| Idh3g | Isocitrate dehydrogenase [NAD] subunit gamma 1, mitochondrial | P70404 | ENSMUSG00000002010 | 1.327 | 0.295 | 1.130 | 0.502 | ↗ |
| Lrpprc | Leucine-rich PPR motif-containing protein, mitochondrial | Q6PB66 | ENSMUSG00000024120 | 1.040 | 0.684 | 1.136 | 0.430 | = |
| Mdh2 | Malate dehydrogenase, mitochondrial | P08249 | ENSMUSG00000019179 | 1.018 | n.s. | 1.667 | 1.224 | ↗ |
| Ndufa10 | NADH dehydrogenase [ubiquinone] 1 alpha subcomplex subunit 10, mitochondrial | Q99LC3 | ENSMUSG00000026260 | 1.484 | 0.317 | 2.144 | 0.683 | ↗ |
| Ndufa5 | NADH dehydrogenase [ubiquinone] 1 alpha subcomplex subunit 5 | Q9CPP6 | ENSMUSG00000023089 | 1.074 | n.s. | 0.939 | 0.417 | n.f. |
| Ndufa6 | NADH dehydrogenase [ubiquinone] 1 alpha subcomplex subunit 6 | Q9CQZ5 | ENSMUSG00000022450 | 1.012 | -0.618 | 1.329 | n.s. | ↗ |
| Ndufa8 | NADH dehydrogenase [ubiquinone] 1 alpha subcomplex subunit 8 | Q9DCJ5 | ENSMUSG00000026895 | 1.092 | n.s. | 1.339 | n.s. | ↗ |
| Ndufb4 | NADH dehydrogenase [ubiquinone] 1 beta subcomplex subunit 4 | Q9CQC7 | ENSMUSG00000022820 | 1.270 | 0.375 | 2.001 | 0.413 | ↗ |
| Ndufs1 | NADH-ubiquinone oxidoreductase 75 kDa subunit, mitochondrial | Q91VD9 | ENSMUSG00000025968 | 1.577 | 0.374 | 2.016 | 0.641 | ↗ |
| Ndufs2 | NADH dehydrogenase [ubiquinone] iron-sulfur protein 2, mitochondrial | Q91WD5 | ENSMUSG00000013593 | 1.142 | 0.216 | 1.163 | 0.519 | ↗ |
| Ndufv2 | NADH dehydrogenase [ubiquinone] flavoprotein 2, mitochondrial | Q9D6J6 | ENSMUSG00000024099 | 1.030 | n.s. | 0.919 | 0.581 | ↗ |
| Oxct1 | Succinyl-CoA:3-ketoacid coenzyme A transferase 1, mitochondrial | Q9D0K2 | ENSMUSG00000022186 | 0.856 | n.s. | 1.549 | 0.567 | ↗ |
| Pdhb | Pyruvate dehydrogenase E1 component subunit beta, mitochondrial | Q9D051 | ENSMUSG00000021748 | 1.004 | 0.621 | 0.868 | 0.973 | ↗ |
| Sdha | Succinate dehydrogenase [ubiquinone] flavoprotein subunit, mitochondrial | Q8K2B3 | ENSMUSG00000021577 | 0.921 | 0.321 | 1.171 | 0.618 | ↗ |
| Uqcrb | Cytochrome b-c1 complex subunit 7 | Q9D855 | ENSMUSG00000021520 | 1.197 | n.s. | 1.511 | 0.731 | n.f. |
| Uqcrfs1 | Cytochrome b-c1 complex subunit Rieske, mitochondrial | Q9CR68 | ENSMUSG00000038462 | 1.398 | -0.435 | 1.008 | 0.807 | ↗ |
| *Other localisation* | | | | | | | | |
| Pfkfb2 | 6-phosphofructo-2-kinase/fructose-2,6-bisphosphatase 2 | P70265 | ENSMUSG00000026409 | 2.060 | 1.987 | 2.306 | 1.014 | n.f. |
| Glul | Glutamine synthetase | P15105 | ENSMUSG00000026473 | 1.084 | 1.436 | 1.234 | 0.947 | n.f. |
| Asns | Asparagine synthetase [glutamine-hydrolyzing] | Q61024 | ENSMUSG00000029752 | 0.761 | 1.635 | 1.424 | 1.098 | = |
| **Other Mitochondrial proteins** | | | | | | | | |
| Aifm2 | Apoptosis-inducing factor 2 | Q8BUE4 | ENSMUSG00000020085 | absent in Dc | n.s. | 1.074 | 0.487 | n.f. |
| Apoo | Apolipoprotein O | Q9DCZ4 | ENSMUSG00000079508 | 1.642 | 0.757 | absent in Mo | 1.038 | n.f. |
| Atad3 | ATPase family AAA domain-containing protein 3 | Q9Z51I | ENSMUSG00000029036 | 0.965 | 0.859 | absent in Mo | 0.978 | ↘ |
| Bdh1 | D-beta-hydroxybutyrate dehydrogenase, mitochondrial | Q80XN0 | ENSMUSG00000046598 | 1.919 | n.s. | 2.249 | 3.216 | n.f. |

| | | | | | | | | |
|---|---|---|---|---|---|---|---|---|
| Glrx5 | Glutaredoxin-related protein 5, mitochondrial | Q80Y14 | ENSMUSG00000021102 | 1.211 | 0.505 | 0.870 | 0.609 | n.f. |
| Hibadh | 3-hydroxyisobutyrate dehydrogenase, mitochondrial | Q99L13 | ENSMUSG00000029776 | 0.827 | -0.654 | 0.804 | 0.315 | ↗ |
| Hsd17b8 | Estradiol 17-beta-dehydrogenase 8 | P50171 | ENSMUSG00000073422 | 3.320 | 0.962 | absent in Mo | n.s. | ↗ |
| Hspd1 | 60 kDa heat shock protein, mitochondrial | P63038 | ENSMUSG00000025980 | 0.832 | 0.769 | 1.273 | 1.204 | = |
| Pdk1 | [Pyruvate dehydrogenase (acetyl-transferring)] kinase isozyme 1, mitochondrial | Q8BFP9 | ENSMUSG00000006494 | absent in Dc | n.s. | 1.491 | 0.791 | n.f. |
| Slc25a11 | Mitochondrial 2-oxoglutarate/malate carrier protein | Q9CR62 | ENSMUSG00000014606 | 0.983 | 0.212 | 0.834 | 0.232 | ↗ |
| Ssbp1 | Single-stranded DNA-binding protein, mitochondrial | Q9CYR0 | ENSMUSG00000029911 | 1.286 | n.s. | absent in Mo | 0.251 | ↗ |
| Tomm40 | Mitochondrial import receptor subunit TOM40 homolog | Q9QYA2 | ENSMUSG00000002984 | absent in Dc | n.s. | 1.243 | 1.003 | ↗ |
| **Translation** | | | | | | | | |
| Abcf1 | ATP-binding cassette sub-family F member 1 | Q6P542 | ENSMUSG00000038762 | 0.866 | 0.296 | 0.839 | n.s. | ↘ |
| Eif1ad | Probable RNA-binding protein EIF1AD | Q3THJ3 | ENSMUSG00000024841 | 0.981 | 0.498 | 1.451 | 0.915 | ↘ |
| Eif2b4 | Translation initiation factor eIF-2B subunit delta | Q61749 | ENSMUSG00000029145 | 1.468 | 0.548 | absent in Mo | 0.358 | ↘ |
| Eif4a2 | Eukaryotic initiation factor 4A-II | P10630 | ENSMUSG00000022884 | 0.933 | n.s. | 0.974 | n.s. | = |
| Gar1 | H/ACA ribonucleoprotein complex subunit 1 | Q9CY66 | ENSMUSG00000028010 | 0.833 | 0.471 | absent in Mo | 0.961 | = |
| Gcn1 | eIF-2-alpha kinase activator GCN1 | E9PVA8 | ENSMUSG00000041638 | 0.810 | 0.546 | 0.986 | n.s. | n.f. |
| Las1l | Ribosomal biogenesis protein LAS1L | A2BE28 | ENSMUSG00000057421 | absent in Dc | 0.920 | 1.065 | 0.653 | ↘ |
| Mrpl40 | 39S ribosomal protein L40, mitochondrial | Q9Z2Q5 | ENSMUSG00000022706 | absent in Dc | n.s. | 0.753 | 0.416 | n.f. |
| Mrpl45 | 39S ribosomal protein L45, mitochondrial | Q9D0Q7 | ENSMUSG00000018882 | absent in Dc | n.s. | 0.899 | 0.755 | n.f. |
| Mrps22 | 28S ribosomal protein S22, mitochondrial | Q9CXW2 | ENSMUSG00000032459 | absent in Dc | 0.864 | 1.672 | 0.955 | ↗ |
| Mrps27 | 28S ribosomal protein S27, mitochondrial | Q8BK72 | ENSMUSG00000041632 | 1.635 | 0.389 | absent in Mo | 0.502 | = |
| Rpl26 | 60S ribosomal protein L26 | P61255 | ENSMUSG00000060938 | 0.893 | -0.337 | 1.018 | n.s. | ↘ |
| Rpl35 | 60S ribosomal protein L35 | Q6ZWV7 | ENSMUSG00000062997 | 1.309 | n.s. | 0.913 | 0.409 | ↘ |
| Utp4 | Cirhin | Q8R2N2 | ENSMUSG00000041438 | 0.944 | 0.543 | absent in Mo | 0.796 | n.f. |
| **Protein transport** | | | | | | | | |
| **Ap1g2** | **AP-1 complex subunit gamma-like 2** | **O88512** | ENSMUSG00000040701 | absent in Dc | n.s. | 1.253 | n.s. | n.f. |
| **Ehd1** | **EH domain-containing protein 1** | **Q9WVK4** | ENSMUSG00000024772 | 0.849 | 0.853 | 0.859 | 1.610 | ↘ |
| **Gga2** | **ADP-ribosylation factor-binding protein GGA2** | **Q6P5E6** | ENSMUSG00000030872 | 2.079 | 1.344 | 1.676 | 1.224 | n.f. |
| **Ipo5** | **Importin-5** | **Q8BKC5** | ENSMUSG00000030662 | 0.915 | 1.261 | 0.877 | 0.445 | = |
| **Lin7c** | **Protein lin-7 homolog C** | **O88952** | ENSMUSG00000027162 | 0.882 | n.s. | 1.391 | n.s. | = |
| Rilpl1 | RILP-like protein 1 | Q9JJC6 | ENSMUSG00000029392 | absent in Dc | 2.264 | 1.761 | n.s. | n.f. |
| Tprg1l | Tumor protein p63-regulated gene 1-like protein | Q9DBS2 | ENSMUSG00000029030 | 3.150 | n.s. | 4.076 | -0.422 | n.f. |
| **Trip11** | **Thyroid hormone receptor interactor 11** | **E9Q512** | ENSMUSG00000021188 | 1.356 | 0.408 | 1.168 | n.s. | n.f. |
| **Vps52** | **Vacuolar protein sorting-associated protein 52 homolog** | **Q8C754** | ENSMUSG00000024319 | 1.096 | n.s. | 1.680 | n.s. | n.f. |
| **Cytokeleton** | | | | | | | | |
| Cyfip2 | Cytoplasmic FMR1-interacting protein 2 | Q5SQX6 | ENSMUSG00000020340 | 0.900 | 1.097 | absent in Mo | n.s. | n.f. |
| Flnb | Filamin-B | Q80X90 | ENSMUSG00000025278 | 1.129 | 1.311 | 1.156 | 1.013 | ↗ |
| Fnbp1l | Formin-binding protein 1-like | Q8K012 | ENSMUSG00000039735 | 1.748 | 2.291 | 0.884 | 1.207 | ↗ |
| Myo1b | Unconventional myosin-Ib | P46735 | ENSMUSG00000018417 | 1.489 | 2.044 | 2.507 | 4.151 | n.f. |
| Nat10 | N-acetyltransferase 10 | Q8K224 | ENSMUSG00000027185 | 0.851 | 0.692 | 2.396 | 0.671 | ↘ |
| Tpm1 | Tropomyosin alpha-1 chain | P58771 | ENSMUSG00000032366 | 1.256 | 1.938 | 0.948 | 1.251 | ↗ |
| ***Tubb6*** | ***Tubulin beta-6 chain*** | ***Q922F4*** | ENSMUSG00000001473 | 1.375 | 1.209 | 1.256 | 1.655 | = |
| **Peptidases/peptidase inhibitors** | | | | | | | | |
| Pgpep1 | Pyroglutamyl-peptidase 1 | Q9ESW8 | ENSMUSG00000056204 | 1.558 | 0.654 | 1.011 | n.s. | n.f. |
| Psmb5 | Proteasome subunit beta type-5 | O55234 | ENSMUSG00000022193 | 1.062 | n.s. | 1.553 | 0.681 | ↗ |
| Rhbdl3 | Rhomboid-related protein 3 | P58873 | ENSMUSG00000017692 | absent in Dc | n.s. | 2.400 | n.s. | n.f. |
| **Serpinb6b** | **NK13** | **O08804** | ENSMUSG00000042842 | 1.749 | 1.912 | 0.807 | 0.996 | n.f. |
| Serpinb8 | Serpin B8 | O08800 | ENSMUSG00000026315 | 1.368 | 2.083 | 1.269 | 2.168 | ↗ |
| **vATPase interactome** | | | | | | | | |
| **Dmxl1** | **DmX-like protein 1** | **Q6PNC0** | ENSMUSG00000037416 | 2.218 | 1.191 | 1.286 | n.s. | n.f. |
| **Oxr1** | **Oxidation resistance protein 1** | **Q4KMM3** | ENSMUSG00000022307 | 2.345 | 1.064 | 1.662 | n.s. | n.f. |
| **Wdr7** | **WD repeat-containing protein 7** | **Q92019** | ENSMUSG00000040560 | absent in Dc | 0.522 | 0.942 | n.s. | n.f. |
| **Micellaneous** | | | | | | | | |
| **Akr1c18** | **Aldo-keto reductase family 1 member C18** | **Q8K023** | ENSMUSG00000021214 | 3.003 | 4.106 | 2.846 | 7.956 | n.f. |
| Pde2a | cGMP-dependent 3,5-cyclic phosphodiesterase | Q922S4 | ENSMUSG00000030653 | 2.264 | 1.784 | absent in Mo | 2.305 | ↘ |
| Pter | Phosphotriesterase-related protein | Q60866 | ENSMUSG00000026730 | 4.076 | 1.196 | 1.510 | 1.055 | ↗ |
| Naa10 | N-alpha-acetyltransferase 10 | Q9QY36 | ENSMUSG00000031388 | absent in Dc | n.s. | 0.845 | 1.120 | = |
| Alad | Delta-aminolevulinic acid dehydratase | P10518 | ENSMUSG00000028393 | 0.867 | n.s. | absent in Mo | n.s. | = |
| **Mast4** | **Microtubule-associated serine/threonine-protein kinase 4** | **Q811L6** | ENSMUSG00000034751 | 1.725 | -2.005 | absent in Mo | -0.556 | n.f. |
| Tep1 | Telomerase protein component 1 | P97499 | ENSMUSG00000006281 | absent in Dc | -0.416 | 1.172 | -0.603 | = |
| Hist1h1b | Histone H1.5 | P43276 | ENSMUSG00000058773 | 0.899 | n.s. | 0.802 | n.s. | ↘ |
| Hist1h1e | Histone H1.4 | P43274 | ENSMUSG00000051627 | 0.868 | n.s. | 1.019 | n.s. | ↘ |
| Map2k2 | Dual specificity mitogen-activated protein kinase kinase 2 | Q63932 | ENSMUSG00000035027 | 0.751 | n.s. | 1.080 | n.s. | ↘ |
| Bag3 | BAG family molecular chaperone regulator 3 | Q9JLV1 | ENSMUSG00000030847 | absent in Dc | n.s. | 1.158 | n.s. | n.f. |
| Birc6 | Baculoviral IAP repeat-containing protein 6 | O88738 | ENSMUSG00000024073 | absent in Dc | n.s. | 0.936 | n.s. | n.f. |
| **Gnl3** | **Guanine nucleotide-binding protein-like 3** | **Q8CI11** | ENSMUSG00000042354 | 1.712 | 1.021 | absent in Mo | 0.838 | ↘ |
| Ndrg3 | Protein NDRG3 | Q9QYF9 | ENSMUSG00000027634 | 0.967 | n.s. | absent in Mo | n.s. | n.f. |
| **Rasa4** | **Ras GTPase-activating protein 4** | **Q6PFQ7** | ENSMUSG00000004952 | 0.886 | 1.778 | 0.907 | 0.608 | n.f. |
| Gsdmdc1 | Gasdermin-D | Q9D8T2 | ENSMUSG00000022575 | 0.901 | 1.075 | 1.299 | 1.674 | = |
| **Ppp1r12b** | **Protein phosphatase 1 regulatory subunit 12B** | **Q8BG95** | ENSMUSG00000073557 | 1.603 | 3.054 | 2.098 | 3.325 | n.f. |
| **Ybx3** | **Y-box-binding protein 3** | **Q9JKB3** | ENSMUSG00000030189 | 1.239 | n.s. | 1.906 | 1.446 | ↘ |
| Ociad1 | OCIA domain-containing protein 1 | Q9CRD0 | ENSMUSG00000029152 | 1.248 | 0.345 | absent in Mo | 0.301 | ↗ |
| Hmgb3 | High mobility group protein B3 | O54879 | ENSMUSG00000015217 | absent in Dc | 1.342 | 2.751 | 1.214 | ↘ |
| Fam91a1 | Protein FAM91A1 | Q3UVG3 | ENSMUSG00000037119 | absent in Dc | n.s. | 1.320 | -0.304 | = |

(a):log2 fold change, n.s.: not significant, n.f.: not found

## Table 2: siRNAs and oligoniucleotides used in this study

| Custom siRNAs | | | | | |
|---|---|---|---|---|---|
| | Name | Gene Symbol | Species | | Sequence |
| | si1077 | Tubb6 | Mouse | | GGCCUGAAGAUGGCCUCCACC |
| | si1373 | Tubb6 | Mouse | | AGCCAUAAGAUGCUACAGUGA |
| | siControl | Luciferase | Firefly | | CUUACGCUGAGUACUUCGA |
| **Dharmacon Smartpool siRNAs** | | | | | |
| Pool Catalog Number | Duplex Catalog Number | Gene Symbol | GENE ID | Gene Accession | Sequence |
| Mouse | | | | | |
| M-046361-01 | D-046361-01 | Mast4 | 328329 | XM_283179 | GAAGGACGCUCGAGAGUUC |
| M-046361-01 | D-046361-02 | Mast4 | 328329 | XM_283179 | CGAAAGAUCCUAAUUGUCA |
| M-046361-01 | D-046361-03 | Mast4 | 328329 | XM_283179 | CAUCCACUGUGAAAGAUUA |
| M-046361-01 | D-046361-04 | Mast4 | 328329 | XM_283179 | GACAGAAGGCGGAAUUUAU |
| M-051664-01 | D-051664-01 | Gnl3 | 30877 | NM_153547 | GUAAGAAGCUGAUACUUGU |
| M-051664-01 | D-051664-02 | Gnl3 | 30877 | NM_153547 | GGCCCUCAUUUAACUAAUA |
| M-051664-01 | D-051664-03 | Gnl3 | 30877 | NM_153547 | GGAGAACUGGCUAAAUUAU |
| M-051664-01 | D-051664-04 | Gnl3 | 30877 | NM_153547 | ACAGGUGCCUCAUUAGGUU |
| M-052134-01 | D-052134-01 | Akr1c18 | 105349 | NM_134066 | GAUGUUGGGUUCUGCCAUA |
| M-052134-01 | D-052134-02 | Akr1c18 | 105349 | NM_134066 | GGACAGAAAUCUUCGGUAC |
| M-052134-01 | D-052134-03 | Akr1c18 | 105349 | NM_134066 | GUGUCUAACUUUAACCGUA |
| M-052134-01 | D-052134-04 | Akr1c18 | 105349 | NM_134066 | GCUGAUAUGUUUAAGGCUC |
| M-044051-01 | D-044051-01 | Ppp1r12b | 329251 | NM_001081307 | CAACAGGGAUUAUAAGAAA |
| M-044051-01 | D-044051-02 | Ppp1r12b | 329251 | NM_001081307 | GGAAUAAGCUCAUCGAGUC |
| M-044051-01 | D-044051-03 | Ppp1r12b | 329251 | NM_001081307 | GAACAGAGCCAAUGUAAAC |
| M-044051-01 | D-044051-04 | Ppp1r12b | 329251 | NM_001081307 | GCUAGAGCUUGCCGAUAUA |
| M-043658-00 | D-043658-01 | Ybx3 | 56449 | NM_011733 | CGACGUCCCUACAACUAUA |
| M-043658-00 | D-043658-02 | Ybx3 | 56449 | NM_011733 | CGUCAGAAAUGGAUAUGGA |
| M-043658-00 | D-043658-03 | Ybx3 | 56449 | NM_011733 | AAACAACCCACGCAAGUAU |
| M-043658-00 | D-043658-04 | Ybx3 | 56449 | NM_011733 | CAACGCUGUUUCACAAGAU |
| M-054591-01 | D-054591-01 | Vps52 | 224705 | NM_172620 | GAUCAGGGAUGAGUACGUA |
| M-054591-01 | D-054591-02 | Vps52 | 224705 | NM_172620 | GGGCCGAGCUCAUCAACAU |
| M-054591-01 | D-054591-03 | Vps52 | 224705 | NM_172620 | GAACAGAUGCUGGGAGCUU |
| M-054591-01 | D-054591-04 | Vps52 | 224705 | NM_172620 | CGAAAUGGAACCAGCAUCA |
| M-045583-01 | D-045583-21 | Oxr1 | 170719 | NM_001130164 | UGAAAUUACCAGCCAAGUA |
| M-045583-01 | D-045583-22 | Oxr1 | 170719 | NM_001130164 | CCUGAAUCUUUCCGACCAA |
| M-045583-01 | D-045583-23 | Oxr1 | 170719 | NM_001130164 | UGUUCAGCCUUGUUGCAUA |
| M-045583-01 | D-045583-24 | Oxr1 | 170719 | NM_001130164 | CCUGAAUGGACAAACGCAU |
| M-065684-02 | D-065684-01 | Kbtbd11 | 74901 | NM_029116 | AGAACUCGGUGGCGCCUUU |
| M-065684-02 | D-065684-02 | Kbtbd11 | 74901 | NM_029116 | CACCUGUAACGGAGAGAUU |
| M-065684-02 | D-065684-03 | Kbtbd11 | 74901 | NM_029116 | CCGUGGAACUCGAGUCUUU |
| M-065684-02 | D-065684-04 | Kbtbd11 | 74901 | NM_029116 | CGGACCAGGUGUAUUGCUA |
| M-057095-01 | D-057095-01 | Lin7c | 22343 | NM_011699 | GGCCUUGGAUUCAAUAUUA |
| M-057095-01 | D-057095-02 | Lin7c | 22343 | NM_011699 | GAAGGUUAAAUUAGUCGUA |
| M-057095-01 | D-057095-03 | Lin7c | 22343 | NM_011699 | GGUAUACGAACAUGUUUAU |
| M-057095-01 | D-057095-04 | Lin7c | 22343 | NM_011699 | GCUACUUUCUGUUAAUGGA |
| M-055471-01 | D-055471-02 | Dmxl1 | 240283 | NM_001081371 | UAGAUUGGCUGGAUGAAUA |
| M-055471-01 | D-055471-03 | Dmxl1 | 240283 | NM_001081371 | GCUUAGCAGUAGCUUAUAA |
| M-055471-01 | D-055471-04 | Dmxl1 | 240283 | NM_001081371 | GGCCUUAGCCGAUACAAUU |
| M-055471-01 | D-055471-17 | Dmxl1 | 240283 | NM_001081371 | GAGGAAGAGAGGUGGCGUA |
| M-043341-01 | D-043341-01 | Ap1g2 | 11766 | NM_001110795 | GAAAGUAGCGAGACCAUGA |
| M-043341-01 | D-043341-02 | Ap1g2 | 11766 | NM_001110795 | GAACAGCUCCAAUGUACGA |
| M-043341-01 | D-043341-03 | Ap1g2 | 11766 | NM_001110795 | GGUCGUUUCUUGCUCAACA |
| M-043341-01 | D-043341-04 | Ap1g2 | 11766 | NM_001110795 | GGUGGAGUGUCUACAGGAA |
| M-044324-02 | D-044324-09 | Trip11 | 109181 | XM_001001171 | CCAAAGACGAGGUCGGCAA |

| | | | | | |
|---|---|---|---|---|---|
| M-044324-02 | D-044324-10 | Trip11 | 109181 | XM_001001171 | GAGAAGAACACCUCGCUAA |
| M-044324-02 | D-044324-11 | Trip11 | 109181 | XM_001001171 | AGAAUGAGGUCCAGCGCUU |
| M-044324-02 | D-044324-12 | Trip11 | 109181 | XM_001001171 | GUGACUAUGAAGAGCGUAU |
| M-056057-01 | D-056057-01 | Wdr7 | 104082 | XM_140391 | GGAAUUAUCGAUCAGCUAA |
| M-056057-01 | D-056057-03 | Wdr7 | 104082 | XM_140391 | CUACUAGAAUACAACCUUA |
| M-056057-01 | D-056057-04 | Wdr7 | 104082 | XM_140391 | GCCGUUACCUUGCCACCUA |
| M-056057-01 | D-056057-17 | Wdr7 | 104082 | XM_140391 | GAAGAGUCACUAACGGAUA |
| M-053228-01 | D-053228-01 | Rasa4 | 54153 | NM_001039103 | GACCGAAGCUGAAGUGUUA |
| M-053228-01 | D-053228-02 | Rasa4 | 54153 | NM_001039103 | CCAGCAAAGUGGAAGUUAA |
| M-053228-01 | D-053228-17 | Rasa4 | 54153 | NM_001039103 | GGAUCUUGUUAGCCGGAAU |
| M-053228-01 | D-053228-18 | Rasa4 | 54153 | NM_001039103 | GCUGCAAGACCUUCGAGAA |
| M-042367-01 | D-042367-01 | Ipo5 | 70572 | NM_023579 | CGAGGAGGCUAGACAAAUG |
| M-042367-01 | D-042367-02 | Ipo5 | 70572 | NM_023579 | UCAAACGGAUGUUAGUUCA |
| M-042367-01 | D-042367-03 | Ipo5 | 70572 | NM_023579 | GGUCAAAUGGCUACAGAUU |
| M-042367-01 | D-042367-04 | Ipo5 | 70572 | NM_023579 | UAAGUCCAAUGCUCCAGUA |
| M-040747-01 | D-040747-01 | Ehd1 | 13660 | NM_010119 | GCACAGGAACCAUGAUAUU |
| M-040747-01 | D-040747-02 | Ehd1 | 13660 | NM_010119 | CAGCCGAGGUUAUGACUUU |
| M-040747-01 | D-040747-03 | Ehd1 | 13660 | NM_010119 | AGAAGGAGAUGCCCAAUGU |
| M-040747-01 | D-040747-04 | Ehd1 | 13660 | NM_010119 | CGAUAUAGCUCGGCUGAUG |
| M-044312-00 | D-044312-01 | Serpinb6b | 20708 | NM_011454 | GGAAUAGCAUCUAAAGAAG |
| M-044312-00 | D-044312-02 | Serpinb6b | 20708 | NM_011454 | GUACUUUUCUCACCUAUAA |
| M-044312-00 | D-044312-03 | Serpinb6b | 20708 | NM_011454 | GAUGAACACAUUGAACUAA |
| M-044312-00 | D-044312-04 | Serpinb6b | 20708 | NM_011454 | CAAUAUAGGUUUUAGGUGU |
| M-040383-01 | D-040383-01 | Gga2 | 74105 | NM_028758 | GGUAUAAGCUGACUUUCAA |
| M-040383-01 | D-040383-02 | Gga2 | 74105 | NM_028758 | CAAAUGACCUUCUCACACA |
| M-040383-01 | D-040383-03 | Gga2 | 74105 | NM_028758 | CAAACCGGCUGAUCAAGAA |
| M-040383-01 | D-040383-04 | Gga2 | 74105 | NM_028758 | GCUCCAAGCUCCCUGCAUU |
| Human | | | | | |
| L-008981-00 | J-008981-06 | TUBB6 | 84617 | NM_032525 | GGAGAUCGAUGGAUAGUCG |
| L-008981-00 | J-008981-07 | TUBB6 | 84617 | NM_032525 | CGAAAGGGCACUACACGGA |
| L-008981-00 | J-008981-08 | TUBB6 | 84617 | NM_032525 | CAAGUCAUGUAAUUAGUCA |
| L-008981-00 | J-008981-09 | TUBB6 | 84617 | NM_032525 | GCACUGGUUUAAUUGUGUU |

Q-PCR primers

| Name | Gene Symbol | Sequence |
|---|---|---|
| Gapdh_L21 | Gapdh | ACAGTCCATGCCATCACTGCC |
| Gapdh_U21 | Gapdh | GCCTGCTTCACCACCTTCTTG |
| Tubb1_F60 | Tubb1 | CTGGGAGGTGATCGGGGAA |
| Tubb1_R181 | Tubb1 | GCACATACTTCTTACCGTAGGCT |
| Tubb2a_F44 | Tubb2a | AGATCGGCGCTAAGTTTTGGG |
| Tubb2a_R193 | Tubb2a | GGATGGCCCGAGGTACATATTT |
| Tubb2b_F78 | Tubb2b | TGAGCATGGTATAGACCCCAC |
| Tubb2b_R232 | Tubb2b | ACCTGACTGAGTCCATTGTGC |
| Tubb3_F89 | Tubb3 | TAGACCCCAGCGGCAACTAT |
| Tubb3_R215 | Tubb3 | GTTCCAGGTTCCAAGTCCACC |
| Tubb4a_F391 | Tubb4a | GGAAAGCTGCGACTGTCTCC |
| Tubb4a_R491 | Tubb4a | ATGATCCTGTCTGGAAACTCCT |
| Tubb4b_F526 | Tubb4b | TCGGACACAGTGGTTGAGC |
| Tubb4b_R677 | Tubb4b | TTCAGGTCACCGTAAGTGGGT |
| Tubb5_F65 | Tubb5 | GATCGGTGCTAAGTTCTGGGA |
| Tubb5_R183 | Tubb5 | AGGGACATACTTGCCACCTGT |
| Tubb6_F154 | Tubb6 | GAGAGGATCAGCGTCTACTACA |
| Tubb6_R281 | Tubb6 | TGTCCGAAGATGAAGTTGTCAG |

**Main figure Legends**

FIG. 1

**Proteomics and transcriptomics of primary myeloid cells. (A-B)** Experimental procedure scheme for SILAC (A) and RNAseq (B) in primary myeloid cells: bone marrow cells were cultured in presence of M-CSF or GM-CSF to obtain Mo and Dc respectively. Oc were obtained by adding RANKL to the Mo cultures. H, M and L isotopic-labeled amino acids were used for Oc, Dc and Mo respectively for SILAC whereas unlabeled amino acid were used for RNAseq. Venn diagrams indicate the distribution of proteins in SILAC for Oc vs Mo, Oc vs Dc and Dc vs Mo comparisons and the distribution of Oc, Dc and Mo transcripts in RNAseq. **(C-D)** Histograms show the distribution of $log_2$ fold changes in proteome (C) and transcriptome (D) for the indicated comparisons (bin size = 0.25).

FIG. 2

**Hierarchical clustering of genes differentially expressed in primary myeloid cells.** Hierarchical clustering of the 12 RNAseq samples (columns) with gene expression heat map of the 9,035 genes (lines) differentially expressed between Oc, Mo and Dc (according to the data in Table S2) with the corresponding genes expression profile clusters on the right.

FIG. 3

**Global transcriptomic and proteomic data analysis to establish the Oc and Dc signatures. (A-B)** Comparative expression profiles of proteins (A) and genes (B) in Oc, Dc and Mo. Colored boxes are the differentially expressed proteins and genes counts, the details of the proteins are in Tables 1, and S4 for Oc and Tables S3 and S5 for Dc, the details of the genes are in Table S2 with the same color code. In blue: more expressed in Oc (Oc signatures): 7+18+61+22+19+18=145 proteins and 137+269+779+7+11+4=1,207 genes, in yellow: more expressed in Dc (Dc signatures): 12+13+47+78+20+12=182 proteins and 336+397+1541+57+45+43=2,419 genes; in red: genes and proteins less expressed in Oc and in grey: genes and proteins less expressed in Dc. Hatched boxes are impossible events. **(C)** Correlation between proteomic and transcriptomic studies: for each mRNA-protein pair and each cell type comparison, graphs show the $log_2$ abundance ratio from SILAC in the x-axis and the corresponding $log_2$ fold change value from RNAseq in the y-axis. R2: correlation coefficients.

FIG. 4

**GO term enrichment analysis and protein networks.**

**(A-D)** Histograms represent $log_2$ fold significant variations of GO terms linked to proteins (A-C) and genes (B-D) more abundant in Oc (A-B) and in Dc (C-D). White and bars correspond to GO terms associated with biological process and black bars to molecular function. GO term details are in Tables S6-9. **(E-G)** Interaction networks among genes overexpressed in Oc: rRNA synthesis and ribosome biogenesis (E), amino acid to tRNA ligation (F) and mitochondrial energy metabolism and translation (G).

FIG. 5.

**RNA interference of potential new regulators of Oc.**

**(A)** Examples of low-resolution images obtained by automated imaging and showing actin and tubulin staining in Oc transfected with control siRNA (siCT) and

siRNA against Dmxl1. Arrows point at the large vacuole-like structures. Scale bar: 50 µm. **(B)** Graph showing the proportion of Oc presenting large vacuole-like structures according to the siRNA transfected, counting at least 100 Oc per experiment and showing the results of 3 to 4 independent experiments depicted with a distinct symbol, with mean % and SEM. **(C)** Confocal images representative of the large vacuole-like structures, from an Oc transfected with siRNA against Vps52. Panels show a single x-y confocal plan with the corresponding x-z and y-z views (46 plans with 377 nm z-steps) along the yellow lines, with staining for actin, CD63 and the overlay with DNA in the right panel. More plans Scale bar = 20 µm.

FIG. 6

**Role of ß tubulin isotype Tubb6 in Oc cytoskeleton organization and resorption activity.**

**(A)** Graph showing mean and SEM mRNA levels normalized to Gapdh of ß-tubulin isotypes in bone marrow macrophages (BMM, black bars) and Oc (grey bars), in three independent experiments and measured by QPCR. **(B)** Graph showing mean and SEM mRNA levels normalized to Gapdh of ß-tubulin isotypes expressed in Oc transfected with the indicated siRNA in five independent experiments and measured by QPCR. **(C)** Representative western blot showing total ß-tubulin and Gapdh expression in Oc transfected with the indicated siRNA. **(D)** Confocal images showing the detail of representative podosome belts in Oc transfected with the indicated siRNA and labeled for actin (red) and vinculin (green). Scale bar: 10 µm. Bar graph shows the mean and SEM % of Oc transfected with the indicated siRNA with a normal podosome belt, counting at least 100 Oc per experiment in 4 (si1077) and 3 (si1373) independent experiments. **(E)** Airyscan confocal images showing the detail of representative podosome belts in Oc transfected with the indicated siRNA and labeled for microtubules (green) and actin (red). Top panels show maximum projections of 13 plans with 172 nm z-steps. Zooms of the boxes areas in the top panels are shown below at different z. Scale bars: 10 µm in top panels and 2 µm in other panels. **(F)** Bar graph comparing the mean and SEM specific resorption activity of Oc transfected with the indicated siRNA and normalized to control siCT, in 3 (si1077) and 4 (si1373) independent experiments. The von Kossa staining of representative wells of one experiment is shown below. **(G)** Confocal images (maximal projection of 7 plans, 210 nm z-step) showing representative podosome belts and the details in a human Oc transfected with the control or TUBB6 siRNA and labeled for actin (red) and DNA (blue). Scale bar: 25 µm. Bar graph shows the % of human Oc transfected with the indicated siRNA with a normal podosome belt, counting at least 100 Oc per experiment in 2 independent Oc preparations from CD14+ human PBMC.

**Supplementary Figure Legneds**

Figure S1

**Differentiation of myeloid cells from mouse bone marrow cells in RPMI medium.**

**(A)** Phase-contrast images of Oc, Dc and Mo differentiated from bone marrow cells in RPMI medium. Scale bars: 50 µm. **(B)** Wide field fluorescence images of Oc and Dc labeled for actin and vinculin. **(C)** RNAseq mapping results for each RNA sample.

Figure S2

**Sample validation and outlier detection in proteomic and transcriptomic studies.**

**(A-B)** Graphical representation of the 2-dimension Principle Component Analysis (PCA) of **(A)** the three samples in the three SILAC experiments and **(B)** the three samples in the four RNAseq experiments. In (A): OM: Oc vs Mo, DM: Dc vs Mo and OD: Oc vs Dc.

Figure S3

**Correlation between protein samples**

Graphs show the comparison of protein log2 abundance ratios between the three samples in the three SILAC experiments. OM: Oc vs Mo, DM: Dc vs Mo and OD: Oc vs Dc.

Figure S4

**Correlation between RNA samples**

Graphs show comparison of gene $\log_{10}$ FPKM between the three samples in the four RNAseq experiments.

Figure S5

**(A) Pikfyve inhibitor.** Representative confocal image of an Oc treated with 1 µM YM201636 for 1 hour showing a single x-y confocal plan top panels and magnification of the boxed area (bottom panels) with staining for actin, CD63 and the overlay with DNA. Scale bars: 20 µm (top panels) and 5 µm (bottem panels). **(B-C) Q-PCR on Oc markers.** Bar graphs show the mean and SEM mRNA levels normalized to Gapdh as measured by QPCR of cathepsin K **(B)** and Src **(C)** in bone marrow macrophages (Mo) and in Oc (black grey bars) transfected with the indicated siRNA, in 3 independent experiments.

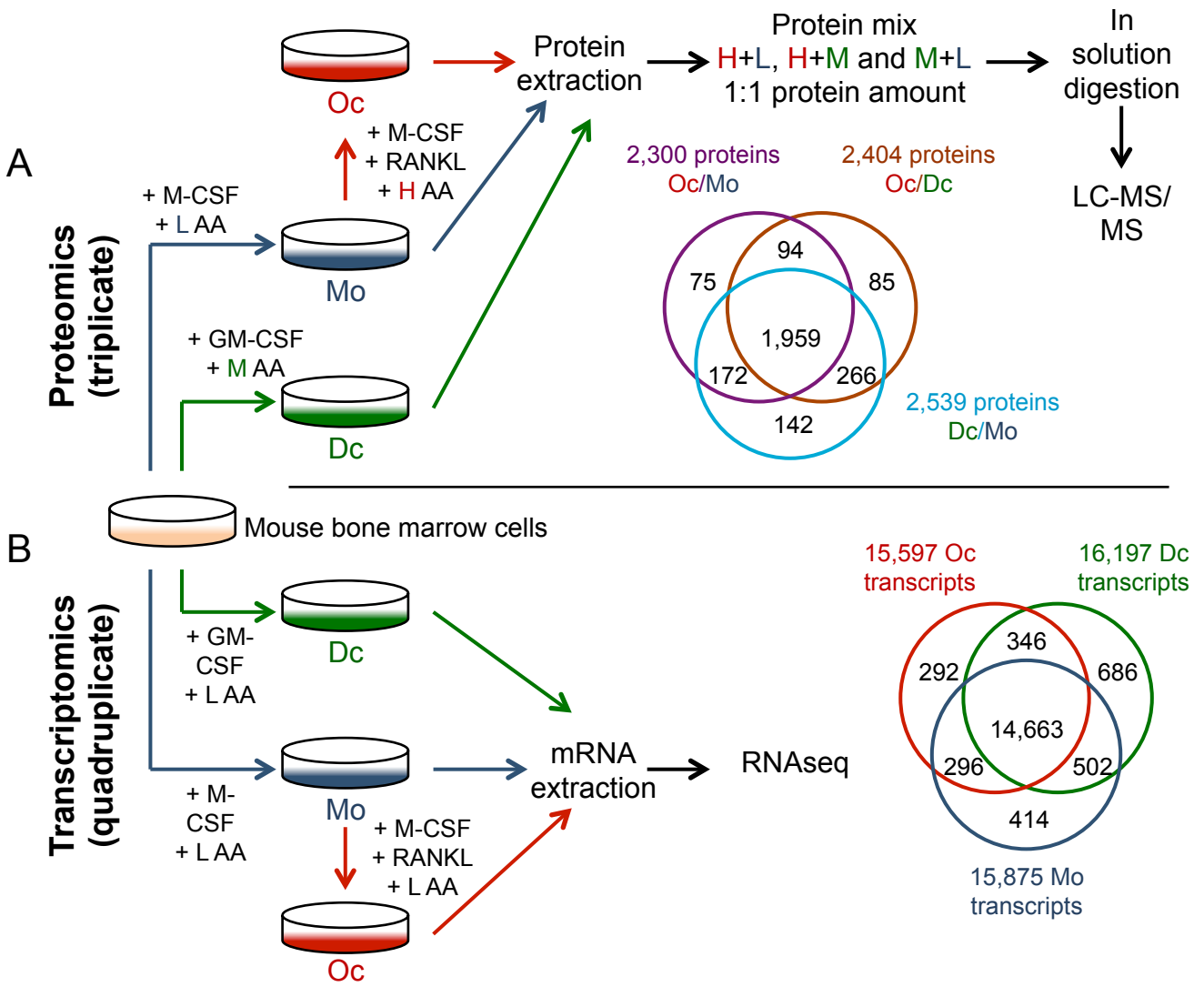


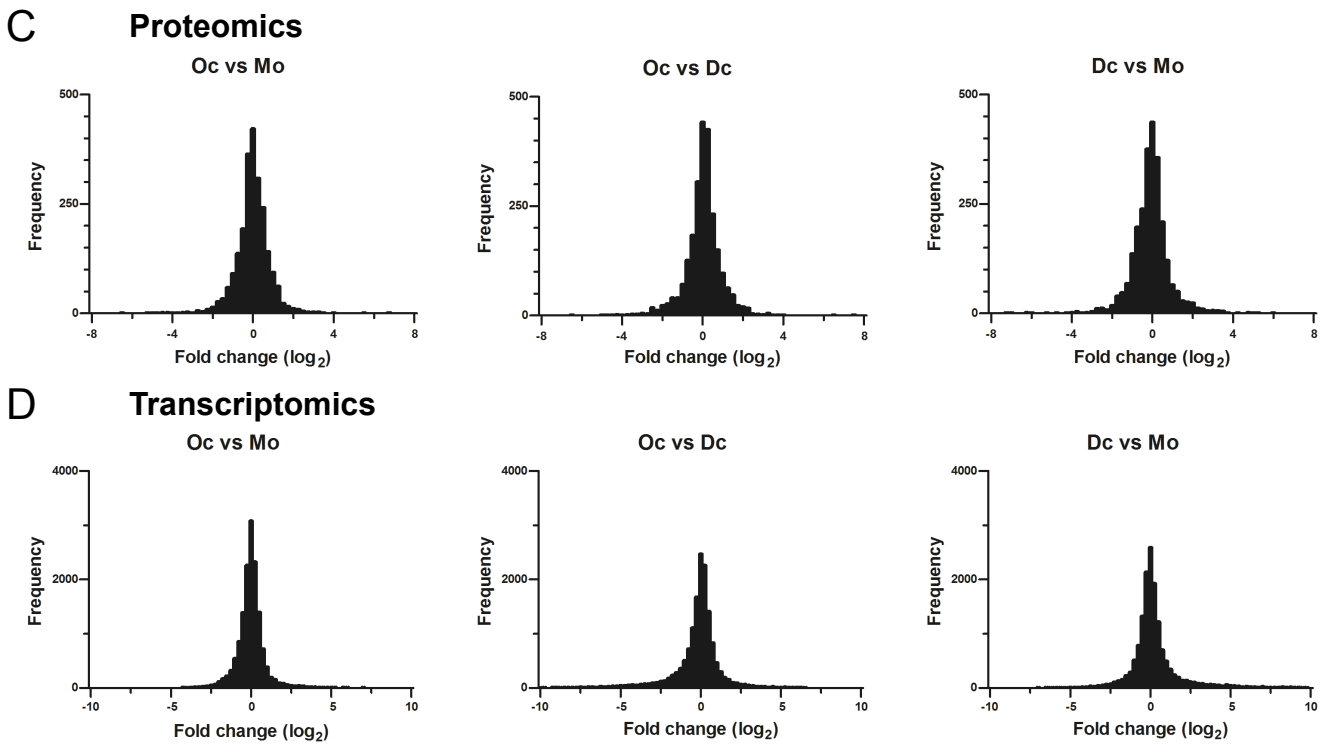


*Marie, Guerit, Figure 1*

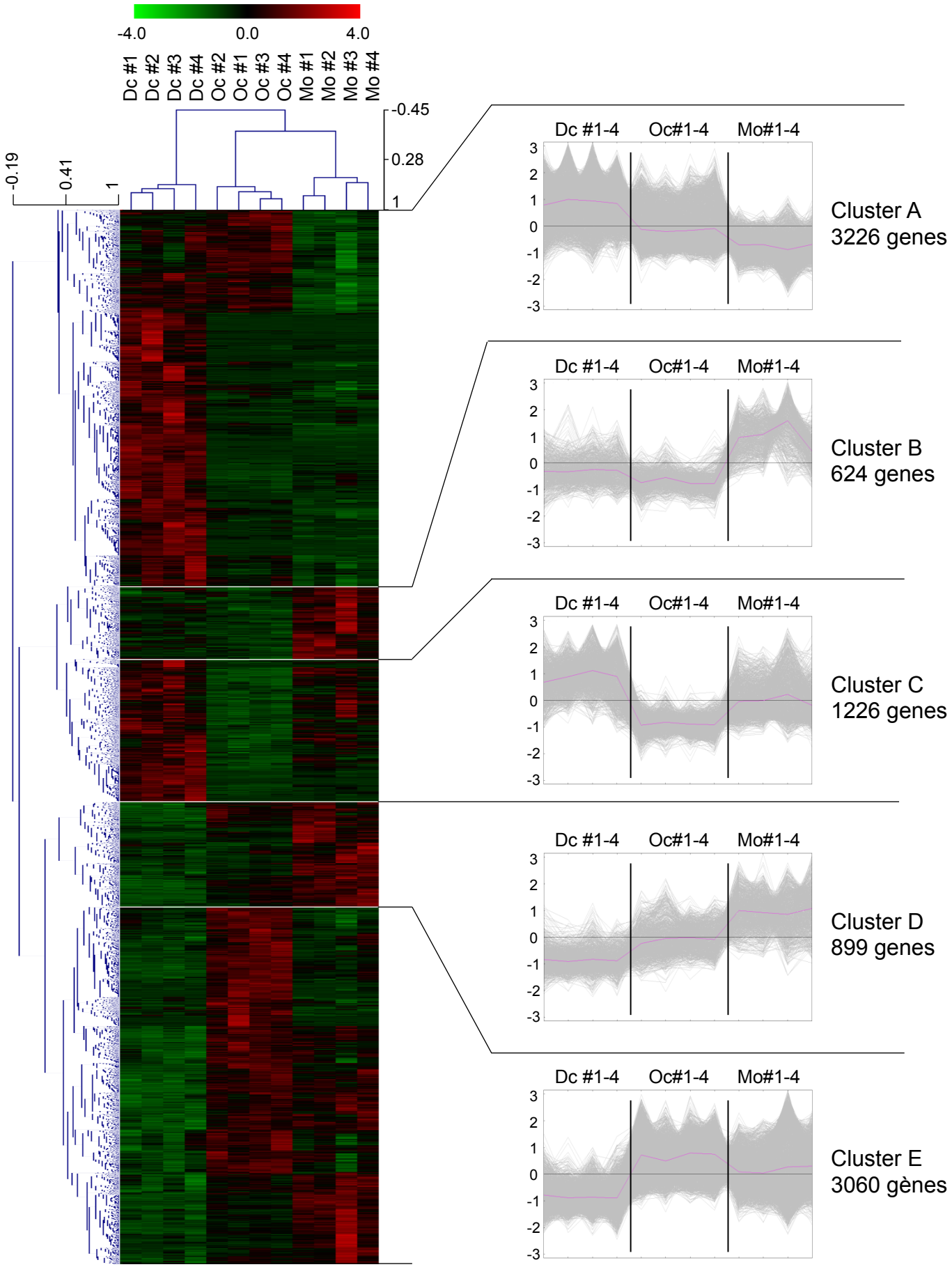


*Marie, Guerit, Figure 2*

A

| | | Oc vs. Dc | | | | | |
|---|---|---|---|---|---|---|---|
| | | absent | Oc > Dc | Oc < Dc | Oc = Dc | | |
| Oc vs. Mo | Oc > Mo | 4 | **7** | **12** | 31 | Dc > Mo | Dc vs. Mo |
| | | 2 | **18** | 2 | 1 | Dc < Mo | |
| | | 9 | **61** | 1 | 97 | Dc = Mo | |
| | | **19** | **22** | 1 | 9 | absent | |
| | Oc < Mo | 2 | 0 | **13** | 6 | Dc > Mo | |
| | | 38 | **19** | **16** | 74 | Dc < Mo | |
| | | 12 | 5 | **51** | 69 | Dc = Mo | |
| | | **15** | 2 | **1** | 7 | absent | |
| | Oc = Mo | 4 | 3 | **47** | 45 | Dc > Mo | |
| | | 36 | **84** | 1 | 92 | Dc < Mo | |
| | | 65 | 72 | 45 | 1087 | Dc = Mo | |
| | | 41 | 18 | 2 | 32 | absent | |
| | absent | **20** | 3 | **78** | 29 | Dc > Mo | |
| | | **35** | **9** | 3 | 12 | Dc < Mo | |
| | | 87 | 17 | 22 | 93 | Dc = Mo | |
| | | | **18** | **12** | 55 | absent | |

B

| | | Oc vs. Dc | | | | | | |
|---|---|---|---|---|---|---|---|---|
| | | Dc = 0 | Oc = 0 | Oc > Dc | Oc < Dc | Oc = Dc | | |
| Oc vs. Mo | Oc > Mo | **7** | | **137** | **336** | 531 | Dc > Mo | Dc vs. Mo |
| | | | | **269** | | | Dc < Mo | |
| | | | | **779** | | 308 | Dc = Mo | |
| | Oc < Mo | **2** | | | **397** | | Dc > Mo | |
| | | | | **387** | **60** | 695 | Dc < Mo | |
| | | | | | **493** | 243 | Dc = Mo | |
| | Oc = Mo | **2** | | | **1541** | 305 | Dc > Mo | |
| | | | | **1196** | | 425 | Dc < Mo | |
| | | | | 411 | 350 | excluded | Dc = Mo | |
| | Oc = 0 | 0 | **57** | | | | Dc > Mo | |
| | | | 0 | | | | Dc < Mo | |
| | | | **1** | | | | Dc = Mo | |
| | Mo = 0 | **4** | **43** | **11** | **45** | 0 | Mo = 0 | |

| Oc signature | Dc signature | Lower in Oc | Lower in Dc |
|---|---|---|---|

C

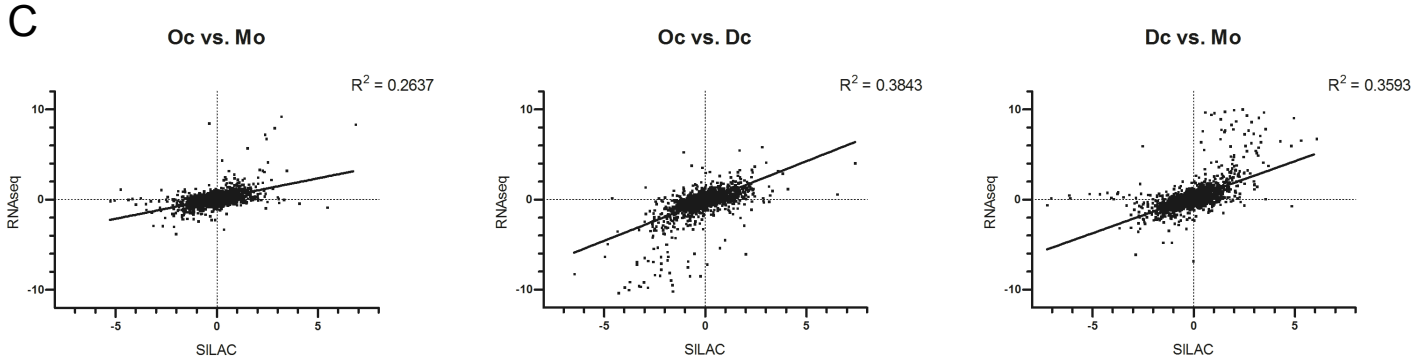


*Marie, Guerit, Figure 3*

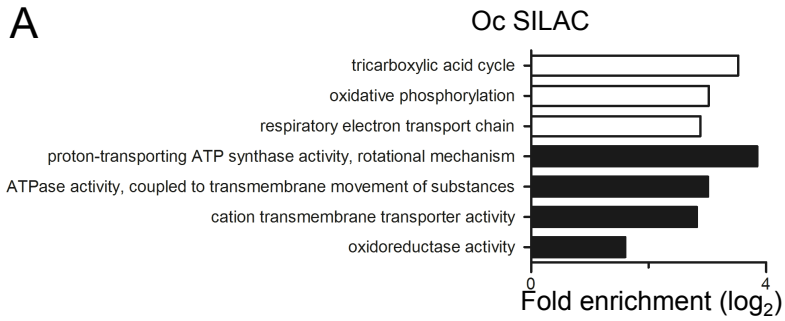


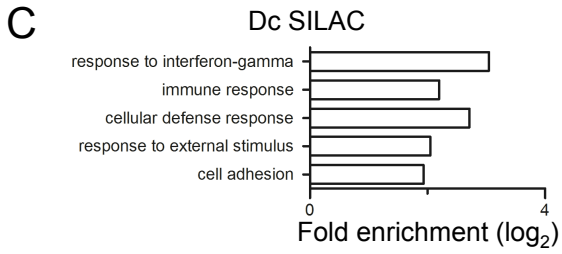


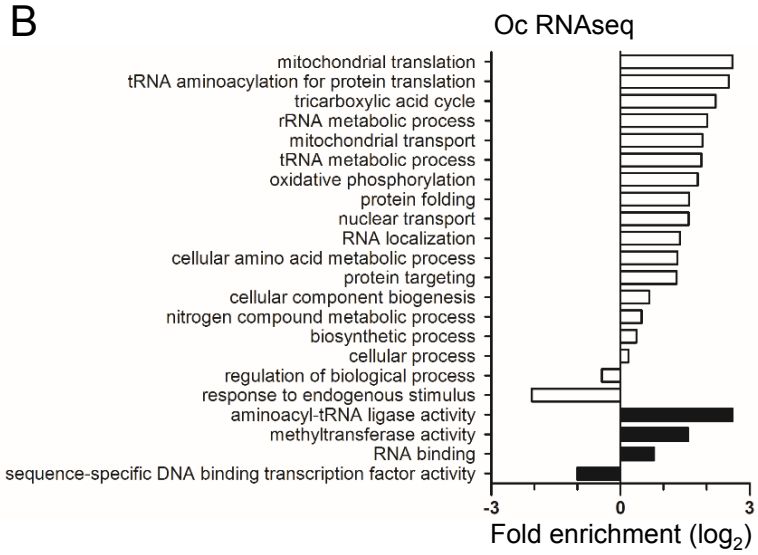


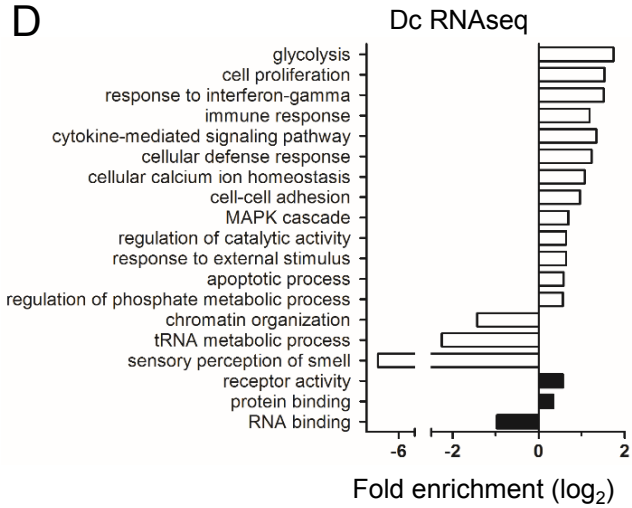


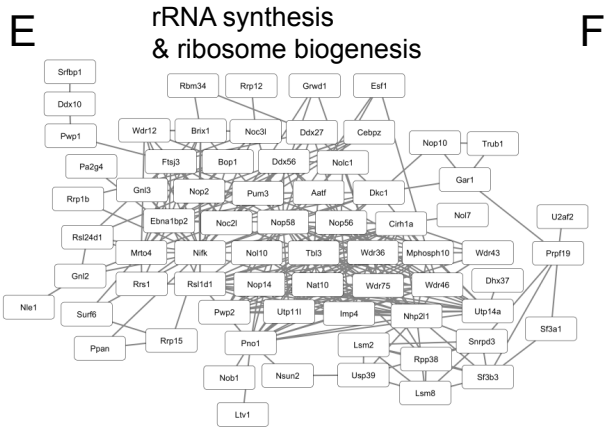


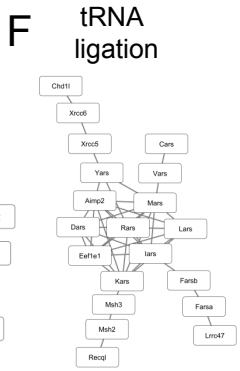


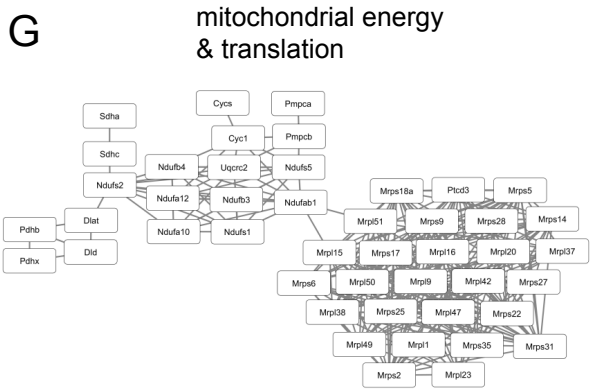


*Marie, Guerit, Figure 4*

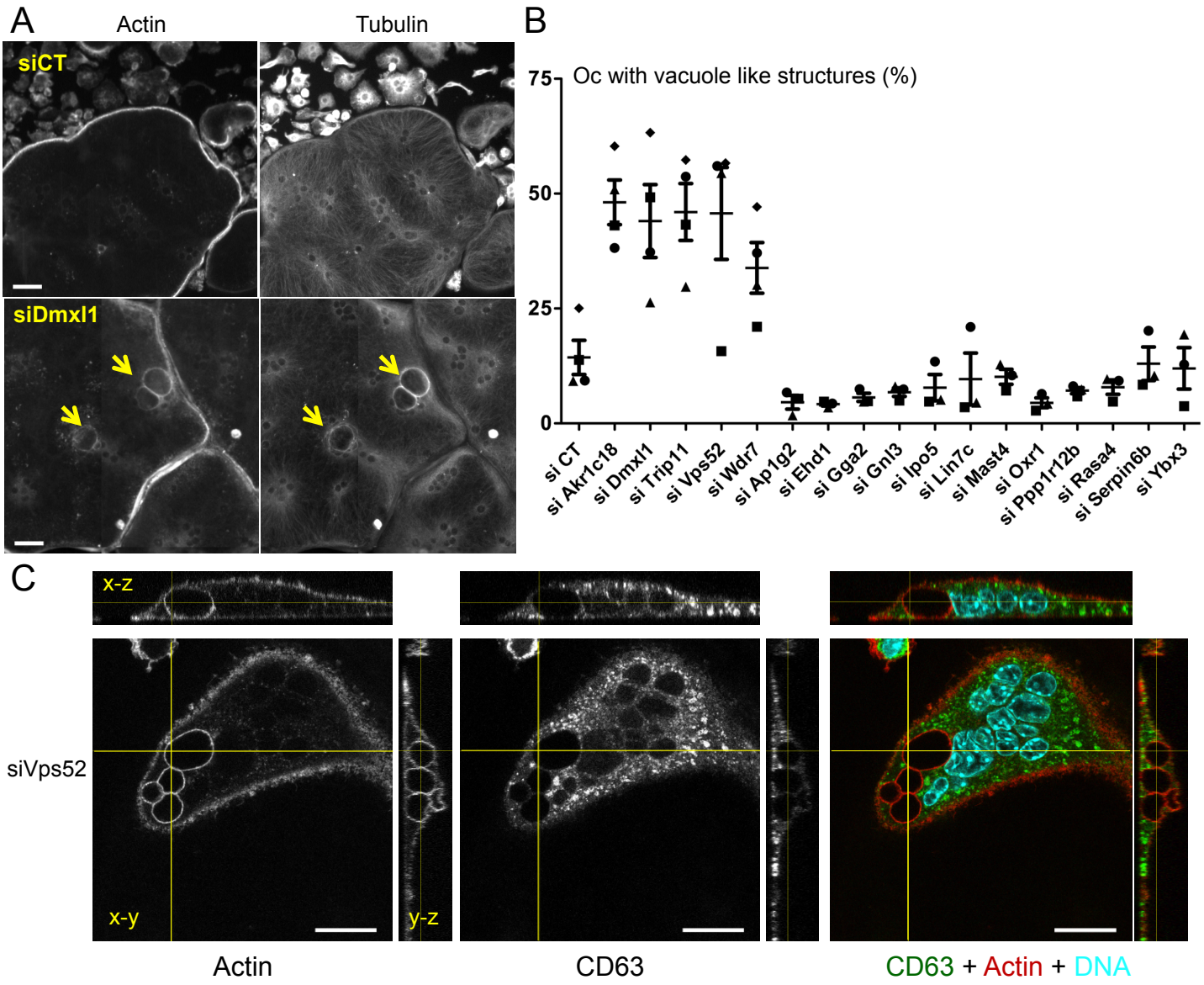


*Marie, Guerit, Figure 5*

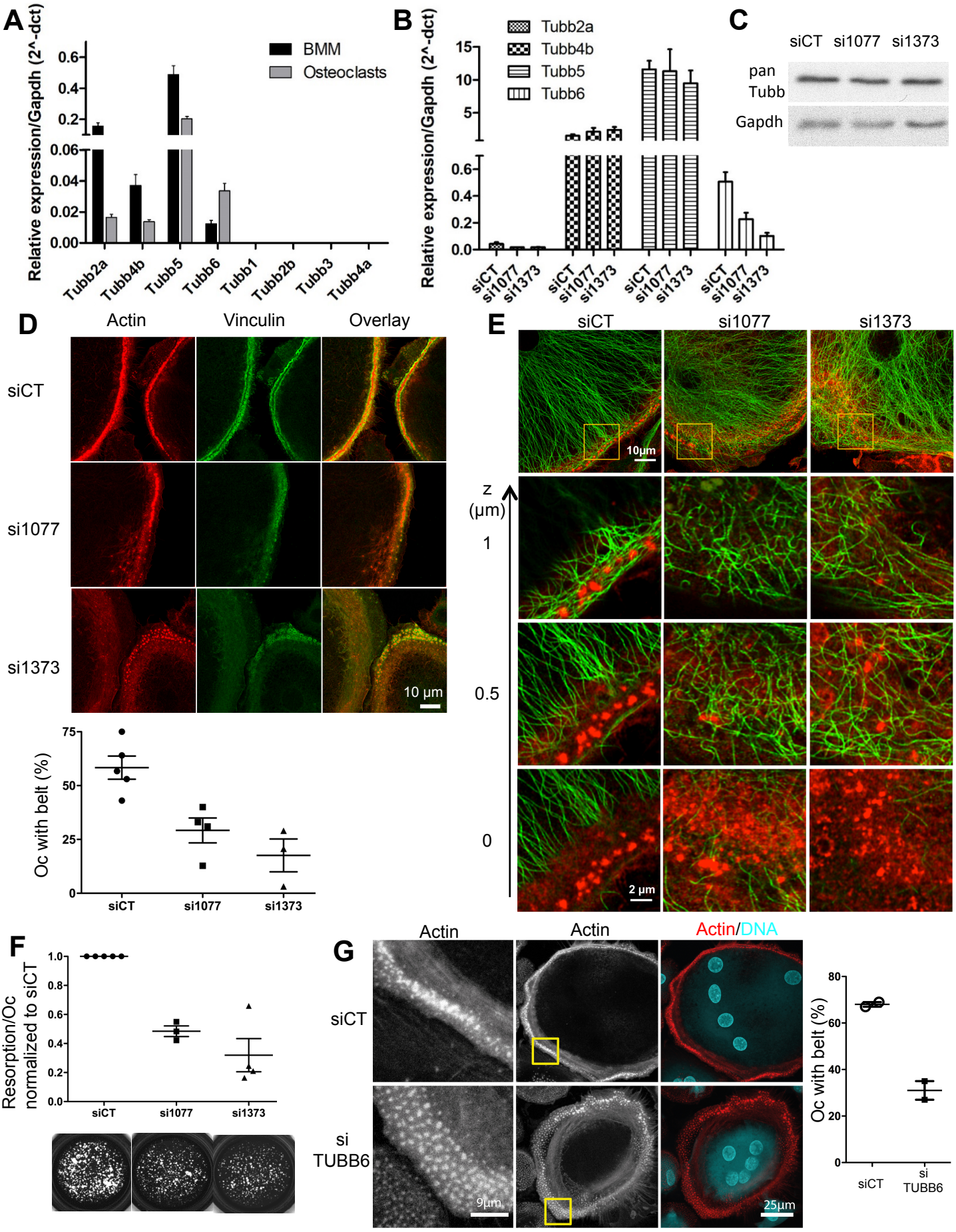


*Marie, Guerit, Figure 6*

**A**

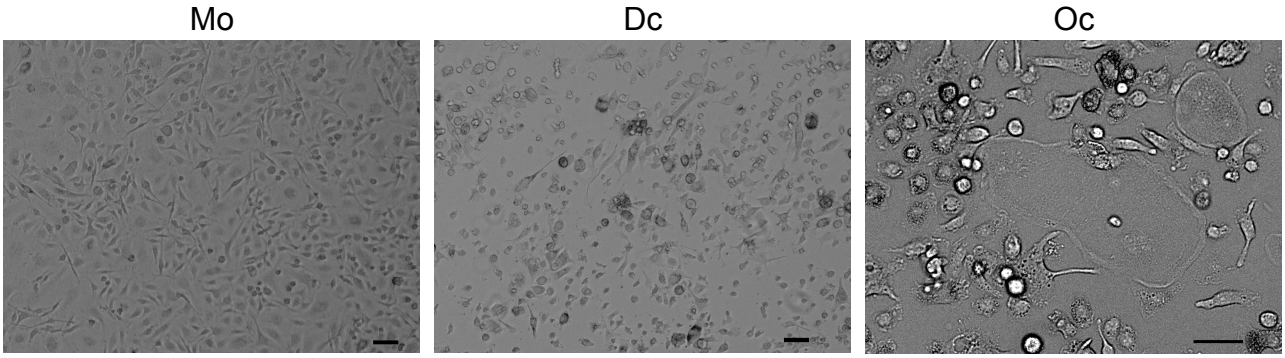


**B**

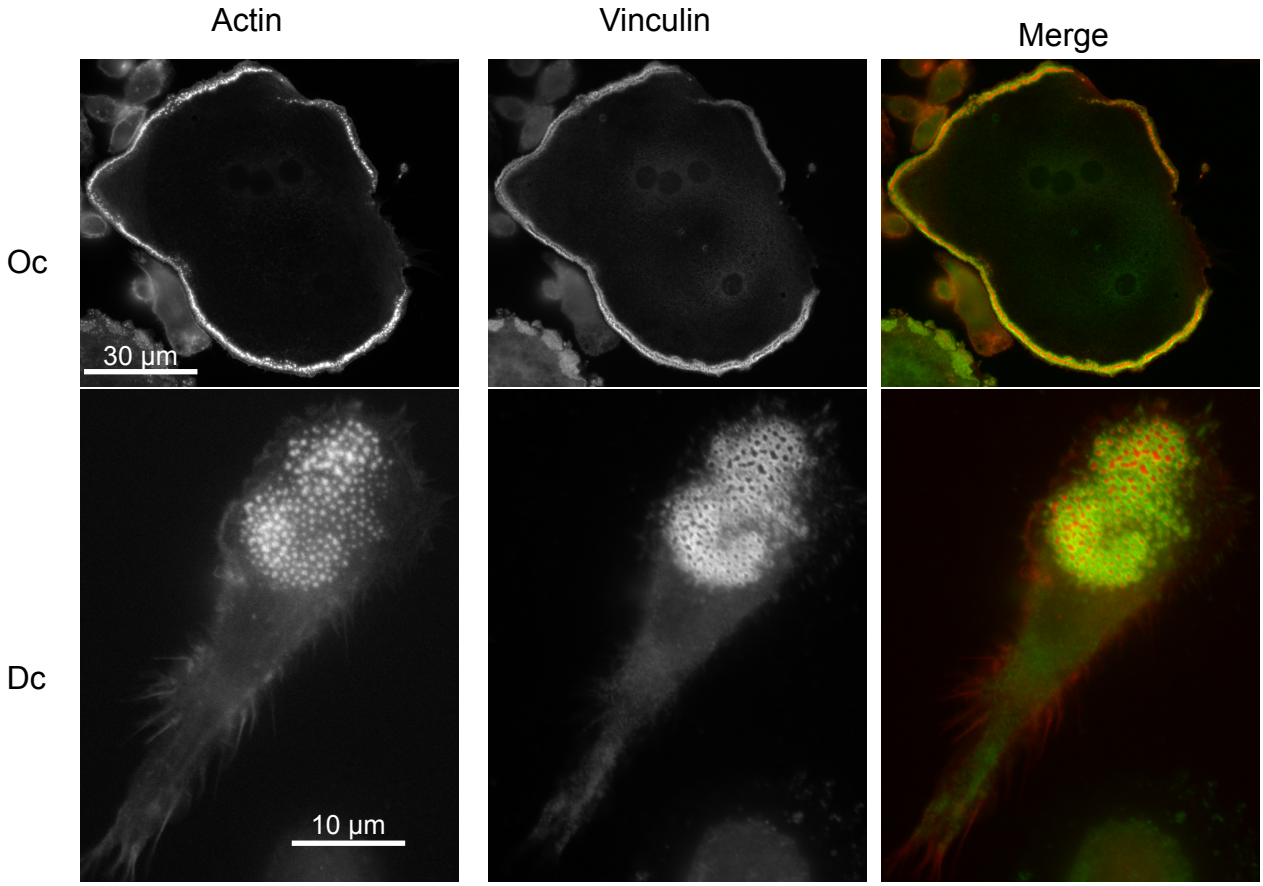


**C**

| Read set | # reads | # mapped reads | % mapped | # secondary mappings | % multiple mappings | % mis |
|---|---|---|---|---|---|---|
| Dendritic cells #1 | 28'888'941 | 28'473'868 | 98.56% | 7'370'517 | 29.20% | 0.25% |
| Dendritic cells #2 | 31'395'783 | 30'935'677 | 98.53% | 9'134'915 | 31.18% | 0.25% |
| Dendritic cells #3 | 26'717'530 | 26'410'012 | 98.85% | 8'218'055 | 32.08% | 0.25% |
| Dendritic cells #4 | 30'753'143 | 30'306'290 | 98.55% | 9'533'862 | 32.43% | 0.28% |
| Macrophages #1 | 33'329'925 | 33'009'000 | 99.04% | 7'345'106 | 25.92% | 0.26% |
| Macrophages #2 | 35'105'037 | 34'766'006 | 99.03% | 7'941'990 | 26.01% | 0.27% |
| Macrophages #3 | 26'939'573 | 26'677'169 | 99.03% | 5'294'294 | 23.62% | 0.26% |
| Macrophages #4 | 36'916'924 | 36'587'806 | 99.11% | 7'797'456 | 25.21% | 0.25% |
| Osteoclasts #1 | 27'850'742 | 27'567'071 | 98.98% | 7'390'420 | 29.88% | 0.25% |
| Osteoclasts #2 | 33'400'695 | 33'045'598 | 98.94% | 8'759'053 | 29.22% | 0.24% |
| Osteoclasts #3 | 27'242'327 | 26'969'591 | 99.00% | 6'676'692 | 28.12% | 0.26% |
| Osteoclasts #4 | 29'306'870 | 28'990'829 | 98.92% | 7'474'601 | 28.61% | 0.26% |

*Marie, Guerit, Supplementary Figure 1*

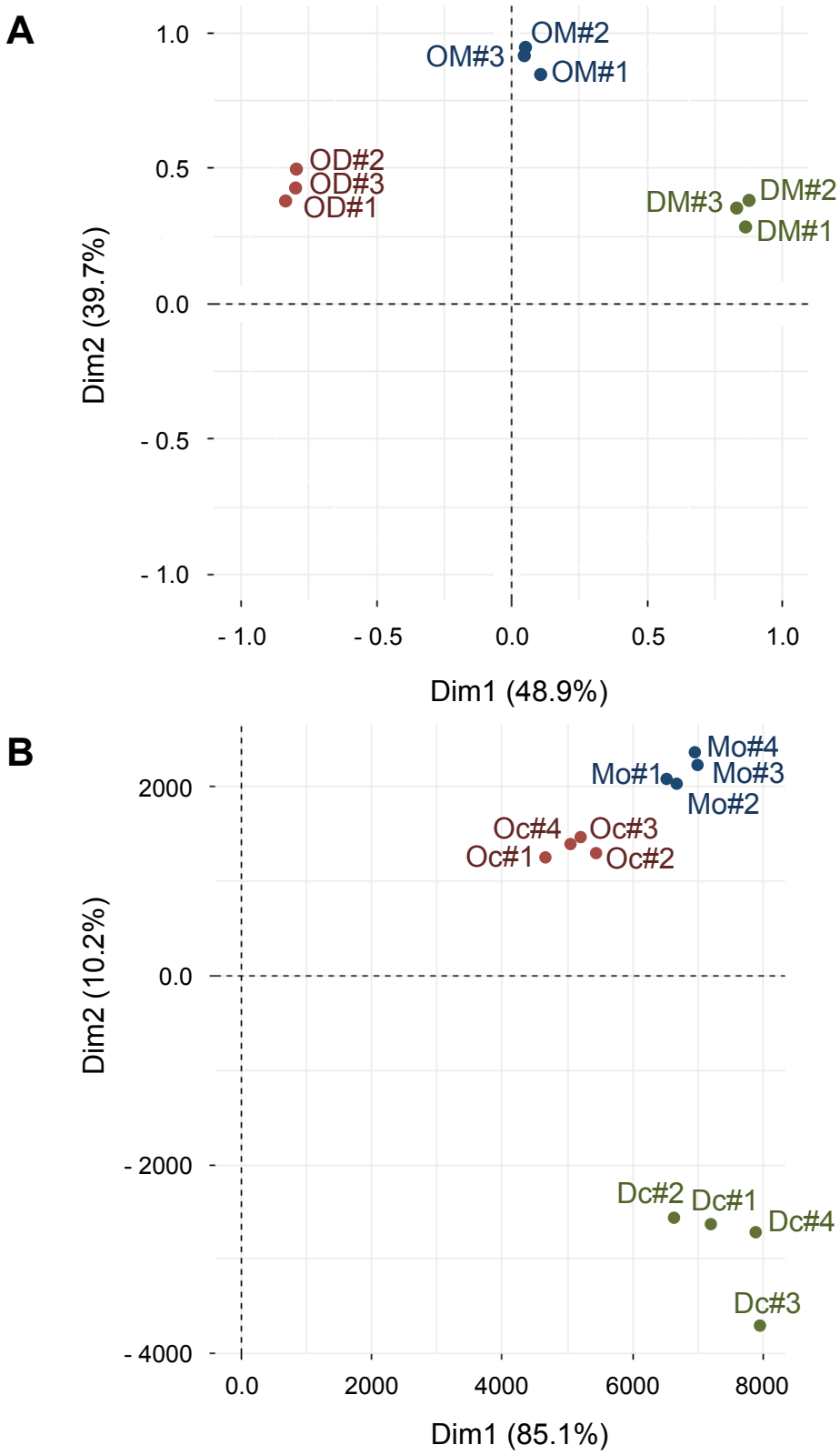


*Marie, Guerit, Supplementary Figure 2*

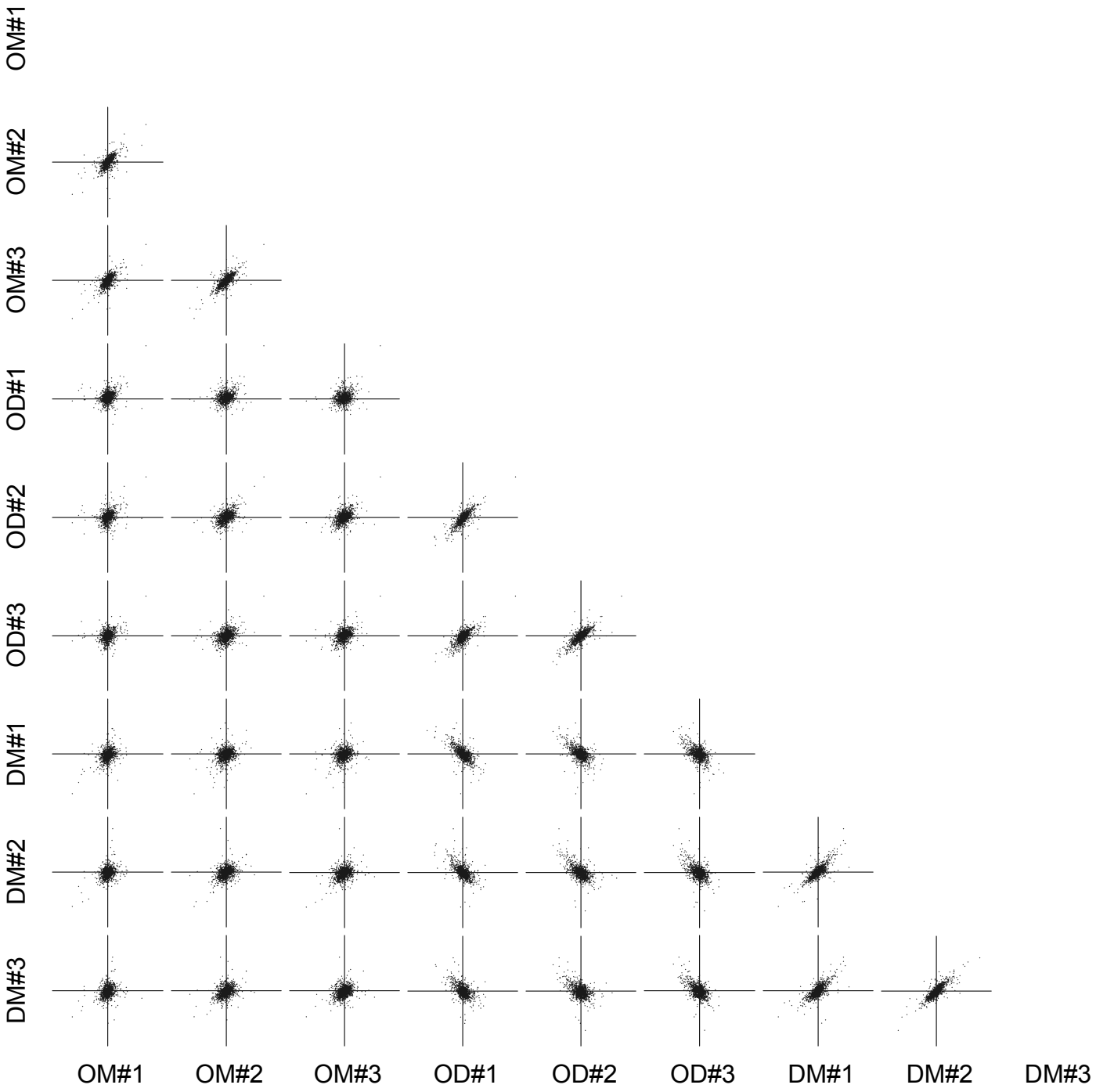


*Marie, Guerit, Supplementary Figure 3*

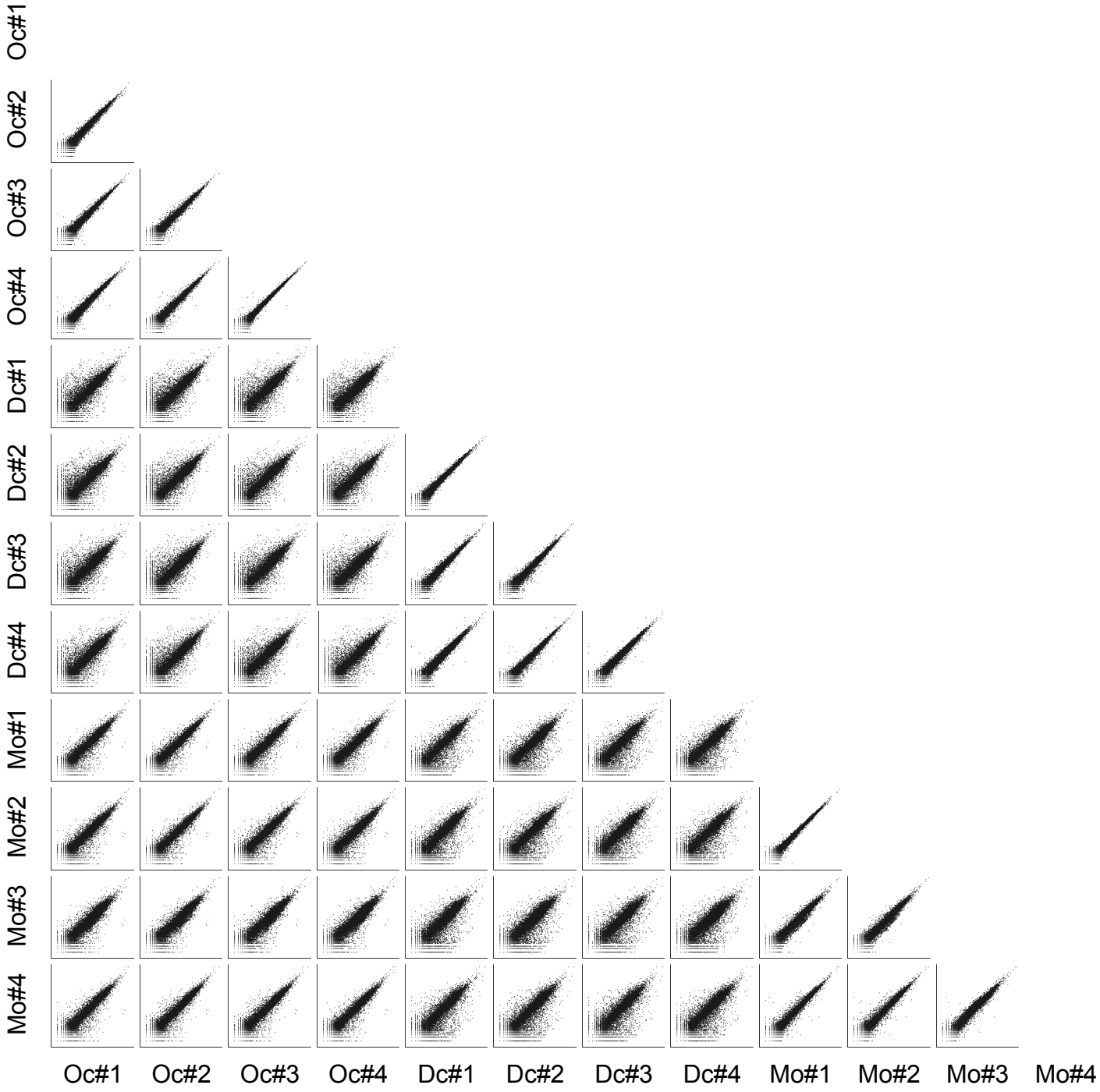


*Marie, Guerit, Supplementary Figure 4*

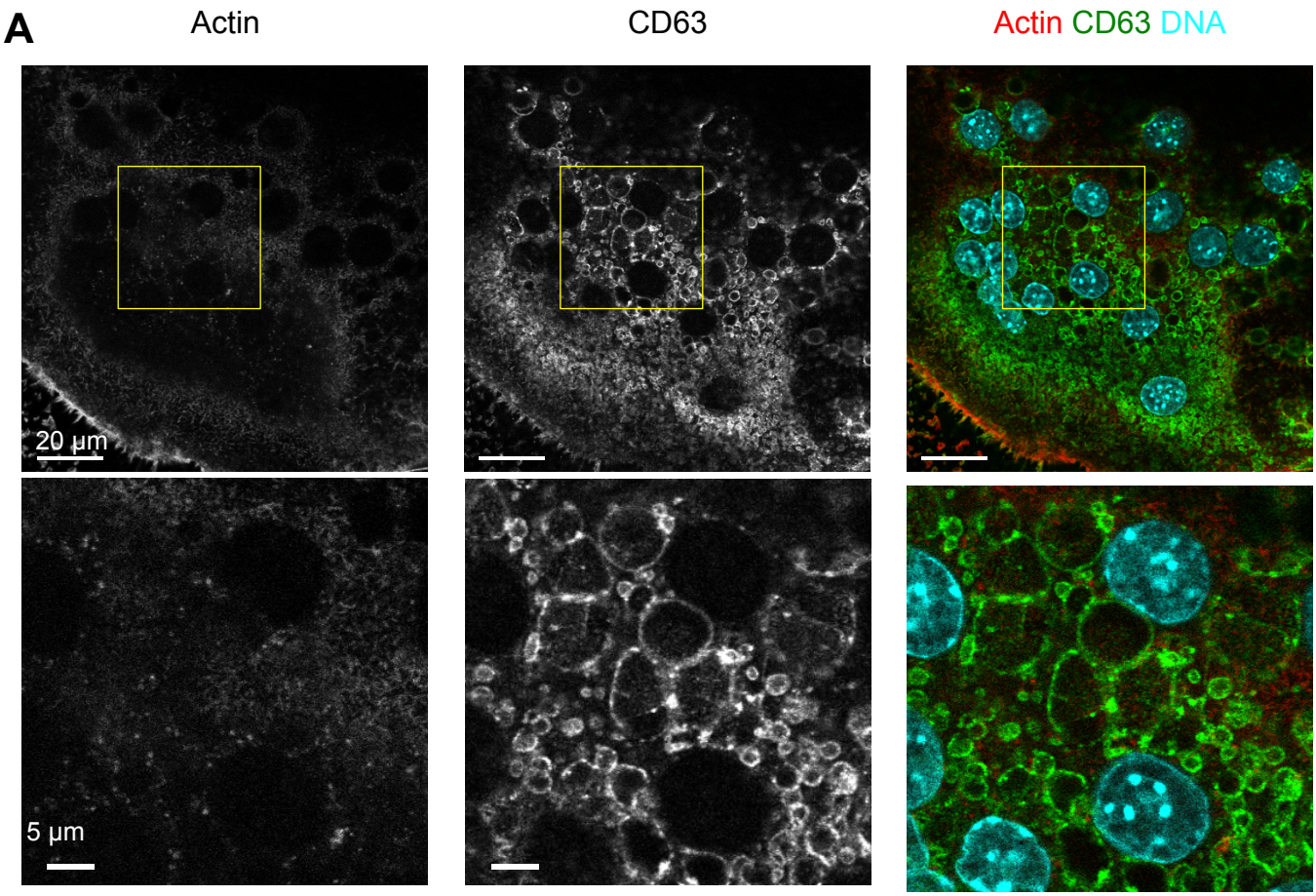


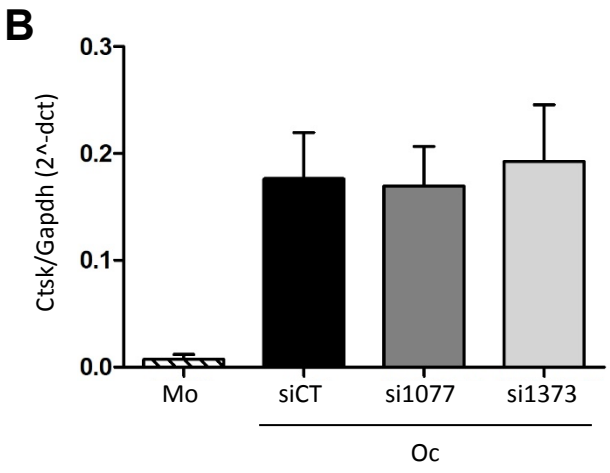


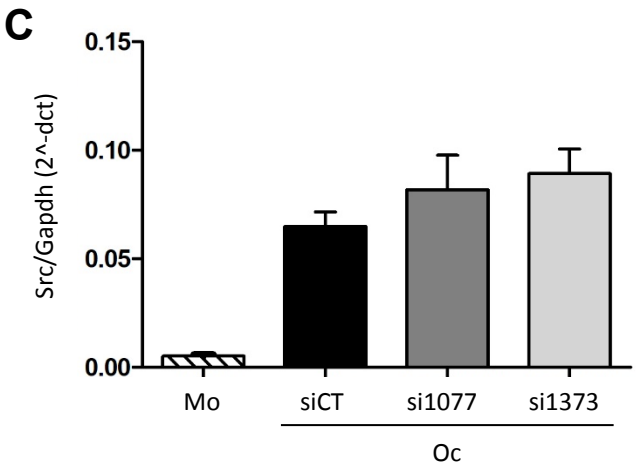


*Marie, Guerit, Supplementary Figure 5*